OPEN ACCESS

Original research

Targeting the oncogenic m6A demethylase FTO suppresses tumourigenesis and potentiates immune response in hepatocellular carcinoma

Ao Chen ,[1,2,3] Vanilla Xin Zhang,[1,2] Qingyang Zhang,[1,2] Karen Man-Fong Sze,[1,2] Lu Tian,[1,2] Hongyang Huang,[1,2] Xia Wang,[1,2] Eva Lee,[1,2] Jingyi Lu,[1,2] Xueying Lyu,[1,2] Man-Fong Joyce Lee,[1,2] Chun Ming Wong ,[1,2] Daniel Wai-Hung Ho,[1,2] Irene Oi-Lin Ng [1,2]

► Additional supplemental material is published online only. To view, please visit the journal online (https://doi.org/10.1136/gutjnl-2024-331903).

[1]Department of Pathology, The University of Hong Kong, Hong Kong, Hong Kong
[2]State Key Laboratory of Liver Research, The University of Hong Kong, Hong Kong, Hong Kong
[3]Department of Biology, Institute of Biology and Medicine, College of Life Science and Health, Wuhan University of Science and Technology, Wuhan, Hubei Province, China

Correspondence to
Professor Irene Oi-Lin Ng, Department of Pathology, The University of Hong Kong, Hong Kong 0000, Hong Kong; iolng@hkucc.hku.hk

AC and VXZ contributed equally.

Received 11 January 2024
Accepted 24 May 2024

To cite: Chen A, Zhang VX, Zhang Q, *et al*. *Gut* Epub ahead of print: [*please include* Day Month Year]. doi:10.1136/gutjnl-2024-331903

ABSTRACT

Objective Fat mass and obesity-associated protein (FTO), an eraser of N^6-methyadenosine (m6A), plays oncogenic roles in various cancers. However, its role in hepatocellular carcinoma (HCC) is unclear. Furthermore, small extracellular vesicles (sEVs, or exosomes) are critical mediators of tumourigenesis and metastasis, but the relationship between FTO-mediated m6A modification and sEVs in HCC is unknown.

Design The functions and mechanisms of FTO and glycoprotein non-metastatic melanoma protein B (GPNMB) in HCC progression were investigated in vitro and in vivo. Neutralising antibody of syndecan-4 (SDC4) was used to assess the significance of sEV-GPNMB. FTO inhibitor CS2 was used to examine the effects on anti-PD-1 and sorafenib treatment.

Results FTO expression was upregulated in patient HCC tumours. Functionally, FTO promoted HCC cell proliferation, migration and invasion in vitro, and tumour growth and metastasis in vivo. FTO knockdown enhanced the activation and recruitment of tumour-infiltrating $CD8^+$ T cells. Furthermore, we identified GPNMB to be a downstream target of FTO, which reduced the m6A abundance of GPNMB, hence, stabilising it from degradation by YTH N^6-methyladenosine RNA binding protein F2. Of note, GPNMB was packaged into sEVs derived from HCC cells and bound to the surface receptor SDC4 of $CD8^+$ T cells, resulting in the inhibition of $CD8^+$ T cell activation. A potential FTO inhibitor, CS2, suppresses the oncogenic functions of HCC cells and enhances the sensitivity of anti-PD-1 and sorafenib treatment.

Conclusion Targeting the FTO/m6A/GPNMB axis could significantly suppress tumour growth and metastasis, and enhance immune activation, highlighting the potential of targeting FTO signalling with effective inhibitors for HCC therapy.

WHAT IS ALREADY KNOWN ON THIS TOPIC

⇒ Fat mass and obesity-associated protein (FTO), the first identified RNA demethylase, plays a pivotal role in regulating N^6-methyadenosine (m6A) modification.
⇒ FTO plays an oncogenic or tumour-suppressive role in different cancers.
⇒ FTO inhibition has been reported to sensitise leukaemic cells to T cell cytotoxicity and overcome hypomethylating agent-induced immune evasion.
⇒ Glycoprotein non-metastatic melanoma protein B (GPNMB) increases the phosphorylation of ERK, AKT and WNT in different models and cell types.
⇒ Syndecan-4 (SDC4) is a receptor protein of $CD8^+$ T cells.

WHAT THIS STUDY ADDS

⇒ FTO is pro-oncogenic in hepatocellular carcinoma (HCC).
⇒ FTO inhibited the activation and recruitment of tumour-infiltrating $CD8^+$ T cells.
⇒ GPNMB was identified as a novel downstream target of FTO-mediated m6A modification.
⇒ GPNMB was packaged into exosomes derived from HCC cells and inhibited $CD8^+$ T cell activation through binding to the surface receptor SDC4 of $CD8^+$ T cells, resulting in cancer immune evasion.
⇒ FTO-GPNMB axis inhibited T cell activation by a cascade of m6A demethylation, small extracellular vesicles/exosomes and immunosuppression.

HOW THIS STUDY MIGHT AFFECT RESEARCH, PRACTICE OR POLICY

⇒ Targeting FTO may provide a new therapeutic approach for treating HCC.
⇒ Targeting FTO may suppress tumour growth and enhance the therapeutic effects of immune checkpoint blockade with anti-PD-1 and sorafenib in HCC.

INTRODUCTION

The N^6-methyladenosine (m6A) modification is the most prevalent chemical modification in eukaryotic mRNA.[1 2] m6A and its regulatory enzymes and reader proteins play critical roles in post-transcriptional gene regulation,[3–6] and their dysregulation has been associated with various diseases, especially cancer. The first identified RNA demethylase, fat mass and obesity-associated protein (FTO), plays a pivotal role in regulating m6A modification[7] and has been

reported to play an oncogenic or tumour-suppressive role in multiple cancers.[8] FTO inhibition has been reported to sensitise leukaemic cells to T cell cytotoxicity and overcome hypomethylating agent-induced immune evasion.[9] Better understanding of the role and underlying molecular mechanisms of FTO in cancers will enhance the development of effective targeted therapeutics against FTO.

Hepatocellular carcinoma (HCC) is a prevalent malignancy worldwide. The role of FTO in HCC is controversial. It has been reported that in HCC, a high level of FTO promoted tumour growth through triggering the demethylation of pyruvate kinase (PKM2) mRNA and accelerating the translation.[10] However, it has also been reported that FTO mRNA and protein levels were significantly downregulated in HCC tumours.[11]

In this study, we found that FTO promoted HCC tumourigenesis and metastasis. Mechanistically, we identified glycoprotein non-metastatic melanoma protein B (GPNMB) as a downstream target of FTO-mediated m6A modification and revealed that GPNMB was packaged into small extracellular vesicles (sEVs) derived from HCC cells. The GPNMB on the sEVs inhibited $CD8^+$ T cell activation through binding to the surface receptor syndecan-4 (SDC4) of $CD8^+$ T cells, resulting in cancer immune evasion. Furthermore, FTO inhibitor, CS2 (NSC368390, also named brequinar), suppressed its oncogenic functions and sensitised HCC cells to immune checkpoint inhibitor anti-PD-1 treatment and enhancing tumour infiltrating $CD8^+$ T cells. The results highlight a new therapeutic approach for HCC and some other cancers by targeting this pathway and sensitising cancer cells to existing immunotherapy and molecular targeted drug treatments.

MATERIALS AND METHODS

A total of 95 patients with primary HCC from The University of Hong Kong-Queen Mary Hospital (HKU-QMH) were included in this study. The details of the materials and methods used in this study including the cell culture techniques, gene manipulation in HCC cell lines, in vitro functional assays, and inhibitor treatments, in vivo animal studies, real-time quantitative PCR (qRT-PCR), next-generation sequencings and statistical analysis are included in online supplemental materials.

RESULTS

Frequent upregulation of FTO RNA demethylase in human HCC and other cancers

According to The Cancer Genome Atlas (TCGA) database, FTO expression was found to be significantly upregulated in seven different solid tumours, including HCC, cholangiocarcinoma, colonic adenocarcinoma, oesophageal squamous carcinoma, head and neck squamous carcinoma, kidney renal clear cell carcinoma and stomach adenocarcinoma (online supplemental figure S1A). This upregulation was confirmed in our in-house HKU-QMH RNA-sequencing (RNA-seq) database with 41 pairs of human HBV-associated HCC (online supplemental figure S1B) and corresponding non-tumour (NT) tissues (figure 1A, left panel) as well as in the TCGA database with 50 paired HCC patient samples (figure 1A, right panel). Additionally, FTO upregulation was verified using qRT-PCR in our expanded HCC cohort consisting of 95 pairs of mainly HBV-associated primary HCC (online supplemental figure S1B), with 40% (n=38/95) showing a ≥twofold upregulation (figure 1B). Immunohistochemistry also revealed higher FTO protein levels in HCC tissues compared with NT tissues (figure 1C). Patients with high FTO expression (twofold cut-off) were found to be significantly associated with poor overall and disease-free survival rates (figure 1D). FTO overexpression was also positively associated with more advanced tumour staging (figure 1E and online supplemental table 1). These findings indicate that FTO is upregulated in HCC and its upregulation is associated with more aggressive tumour and poorer prognosis.

Knockdown of FTO inhibited HCC progression and cell stemness properties

In our panel of human HCC cell lines, FTO was found to be highly expressed in HCC cell lines (MHCC97L (97L; authenticated to have no contamination; see online supplemental figure S1C) and HepG2) as compared with an immortalised normal liver cell line, while the lowest expression was observed in PLC/PRF/5 (PLC) cell line (online supplemental figure S1D). Using two independent short hairpin RNA (shRNA) sequences (shFTO#1 and #2), FTO stable knockdown (KD) was established in 97L and HepG2 cells (figure 2A, online supplemental figure S1E).

FTO KD significantly suppressed HCC cell proliferation (figure 2B), migration and invasion (figure 2C). To investigate whether silencing FTO could suppress tumour growth and progression of HCC cells in vivo, we employed an orthotopic mouse xenograft model. Luciferase-labelled 97L cells with FTO KD or non-target control (NTC) were injected into the livers of nude mice (figure 2D). A significant reduction in bioluminescence signals (figure 2E,F) and tumour mass (figure 2G) was observed on FTO KD. Additionally, a lower lung metastasis rate was detected in the FTO KD group (figure 2H). These findings demonstrate that FTO plays a crucial role in HCC cell proliferation, migration and invasion in vitro and tumour growth and progression in vivo. In addition, the effects of FTO KD on tumourigenicity were examined. FTO KD could significantly inhibit colony formation and sphere formation (self-renewal ability in vitro) in HCC cells (figure 2I,J). Moreover, FTO KD substantially downregulated the expression of cancer stemness genes, in these HCC cells (online supplemental figure S1F). A limiting dilution assay to assess tumour initiation ability was performed by subcutaneously injecting various numbers of 97L cells into nude mice (figure 2K). The results showed a significantly reduced incidence rate of tumour initiation on FTO KD ($p<0.001$) (figure 2L,M). The suppressive effect on tumour formation was more evident for sequence shFTO#1, especially when lower numbers of HCC cells were injected. These findings revealed that FTO KD not only impedes tumour initiation but also suppresses tumour growth and progression in HCC.

KD of FTO inhibited tumour growth and enhanced infiltration, activation and recruitment of tumour-infiltrating $CD8^+$ T cells

We queried whether the tumour-suppressive effects of FTO KD observed in immunodeficient mice were also present in immunocompetent mice. To this end, we used an orthotopic liver injection model and injected luciferase-labelled mouse hepatoma cells Hepa1-6 into immunocompetent C57BL/6 mice (figure 3A). On FTO KD, a significant reduction in bioluminescence signals (figure 3B) and tumour mass (figure 3C) was observed. Importantly, there were significantly increased numbers of tumour-infiltrating immune cells ($CD45^+$) and cytotoxic $CD8^+$ T cells ($CD45^+$ $CD8^+$) in the tumours with FTO KD. This was accompanied by a significant reduction in PD-1^+ exhausted $CD8^+$ T cells (figure 3D). Although the total tumour-infiltrating macrophages ($CD45^+$ $F4/80^+$) remained unchanged on FTO KD (online supplemental figure S2A), there was a trend of an increase in

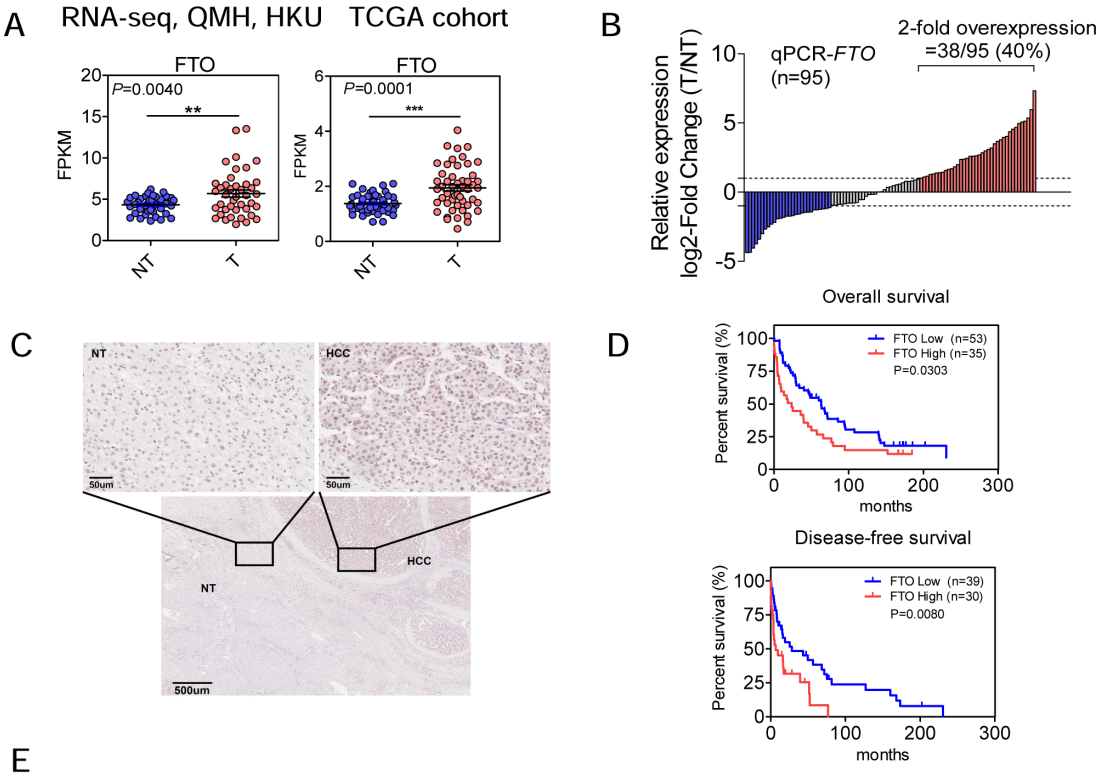

E

Parameters	FTO overexpression (n=37)	FTO normal and underexpression (n=56)	*P* *
Tumor-node-metastasis staging			**<0.0001***
I-II	2 (2.4%)	25 (30.1%)	
III-IV	31 (37.3%)	25 (30.1%)	

* Fisher exact test

Figure 1 Frequent upregulation of FTO RNA demethylase in human HCC. (A) The RNA-seq data demonstrates that FTO is frequently upregulated in our in-house HKU-QMH HCC cohort (n=41) and TCGA paired HCC cohort (n=50). (B) The mRNA level of FTO was highly expressed in 40% of 95 pairs of patients' HCC samples when compared with non-tumourous liver tissues. (C) Representative immunohistochemical images of FTO in HCC tissue and non-tumourous liver tissue. (D) The high FTO expression was associated with a poorer overall survival of patients with HCC. (E) With a cut-off of twofold upregulation by qPCR, overexpression of FTO was significantly associated with more advanced tumour stages (p=0.000029). t-test, mean±SD, *p<0.05, **p<0.01, ***p<0.001. FTO, fat mass and obesity-associated protein; HCC, hepatocellular carcinoma; HKU, University of Hong Kong; QMH, Queen Mary Hospital; qPCR, quantitative PCR; NT, non-tumour; TCGA, The Cancer Genome Atlas.

antitumoural M1 macrophages ($CD86^+$) (online supplemental figure S2B), but not pro-tumoural M2 macrophages ($CD163^+$) (online supplemental figure S2C). These findings suggest that FTO KD enhances the infiltration of cytotoxic T cells and anti-tumoural macrophages to inhibit HCC tumour growth in immunocompetent mice.

To further investigate the effect of FTO KD on T cell activation, $CD8^+$ T cells were isolated from the peripheral blood mononuclear cells (PBMCs) of healthy donors and cocultured with human HCC cell line MHCC97L with or without FTO KD. There was a significant increase in $CD44^+CD62L^-$ effector memory T cells on FTO silencing, as compared with the NTC group (figure 3E). FTO KD also enhanced the proliferation of human $CD8^+$ T cells, as demonstrated with carboxyfluorescein succinimidyl ester staining, followed by gating the counts of proliferated cells using FlowJo software and normalised to the NTC group (online supplemental figure S2D). This indicates that FTO may suppress T cell activation and proliferation in the HCC tumour microenvironment.

To strengthen this observation, we used the human monocyte cell line THP-1 and induced the cells to M0 differentiation and further to M1 or M2 polarisation.[12] M1 or M2 macrophages were then cocultured with HCC cells with or without FTO depletion. A significant promotion in the migratory ability of M1 macrophages was observed when they were cocultured with FTO KD 97L cells, while a reduction was seen with M2 macrophages on such coculture (figure 3F,G). Consistently, there was an increase in the expression of M1 markers, including CD68, CD80 and CD86, while decreased expression of CD204, an M2 marker, was seen with one of the FTO KD sequences (online supplemental figure S2E). These findings suggest that FTO KD promotes the activation and proliferation of cytotoxic T cells and enhances the migratory ability of antitumoural M1 macrophages in the HCC tumour microenvironment.

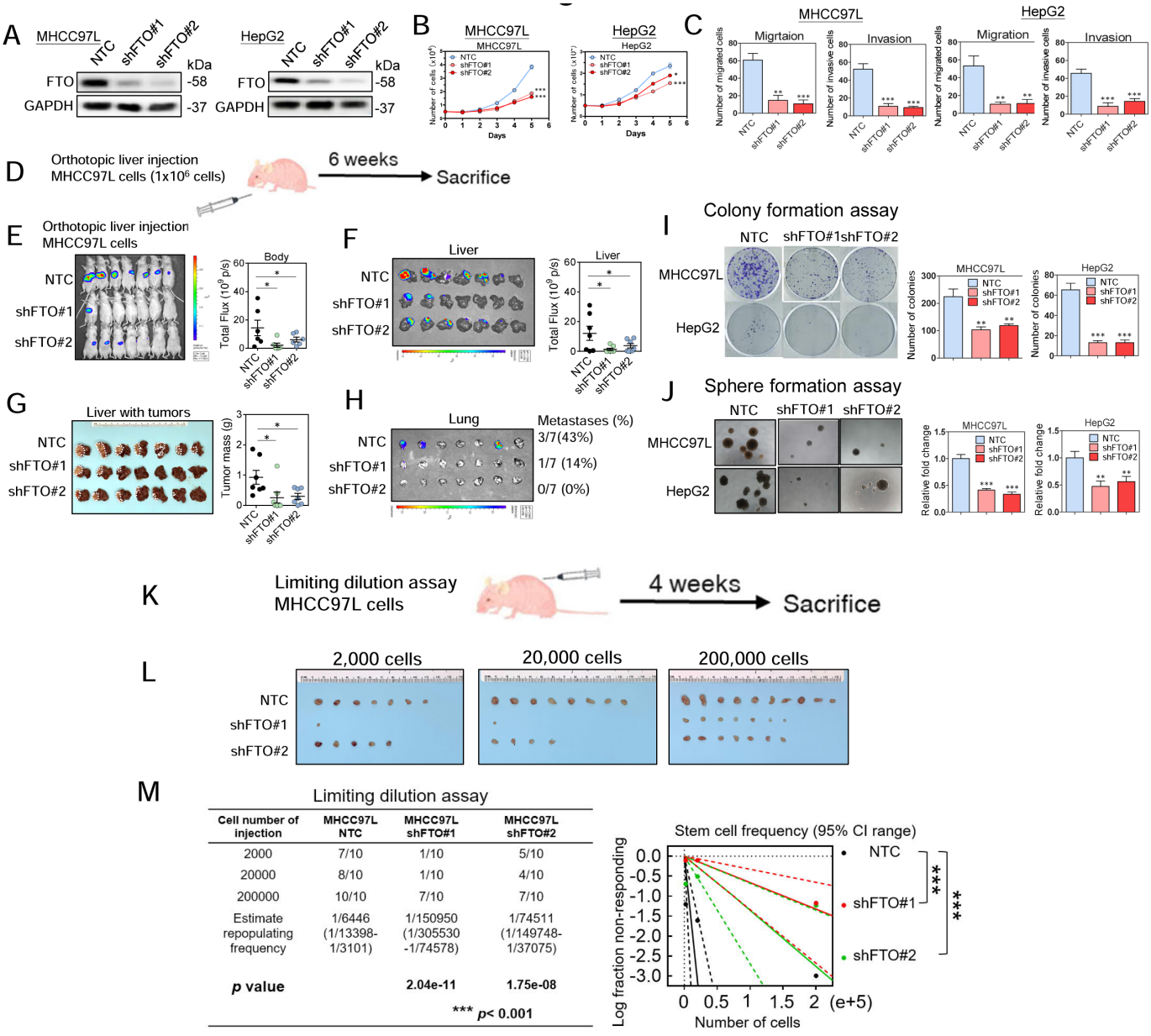

Cell number of injection	MHCC97L NTC	MHCC97L shFTO#1	MHCC97L shFTO#2
2000	7/10	1/10	5/10
20000	8/10	1/10	4/10
200000	10/10	7/10	7/10
Estimate repopulating frequency	1/6446 (1/13398-1/3101)	1/150950 (1/305530 -1/74578)	1/74511 (1/149748-1/37075)
***p* value**		**2.04e-11**	**1.75e-08**

*** *p*< 0.001

Figure 2 Knockdown (KD) of fat mass and obesity-associated protein (FTO) suppressed hepatocellular carcinoma cell proliferation, metastasis and self-renewal ability. (A) Western blotting showed successful stable KD of FTO in 97L and HepG2 cells. (B) Significant inhibition on cell proliferation on FTO KD. (C) The number of migrated or invaded cells was significantly reduced on FTO KD (n=3). (D) A schematic representation of the orthotopic injection model. (E) Bioluminescent images of nude mice subjected to orthotopic liver injection of 97L-luc cells (non-target control (NTC), shFTO#1 and shFTO#2) (n=7 for each group). (F) Bioluminescent images of livers and quantification of their bioluminescent intensities. (G) Dissected livers with tumours from the three groups of mice and weights of the dissected tumours. (H) Bioluminescent images of lung tissues and metastasis rate to lungs. (I) Colony formation assay and (J) sphere formation assay on FTO KD and NTC groups in 97L and HepG2 cells (n=3). (K) In vivo limiting dilution assay showing rates of tumour formation from subcutaneous injection of 2×10^3, 2×10^4 and 2×10^5 97 L cells. (L), (M) The tumour incidence rate for each group was recorded at the end of the experiments after 4 weeks. Tumour initiating capacity was analysed by the CIs with the formula of CI=1/(stem cell frequency). t-test, mean±SD, *p<0.05, **p<0.01, ***p<0.001.

RNA-seq and m6A-sequencing identified GPNMB as a downstream target of FTO-mediated m6A modification

To determine the molecular mechanism of FTO in HCC, RNA-seq was performed in FTO KD HCC cells. There were 60 upregulated genes and 133 downregulated genes when compared with NTC by two independent shRNAs in both HepG2 and 97L cells (figure 4A, online supplemental figure S3A). GO biological processes annotation analysis revealed that the upregulated and downregulated differentially expressed genes were significantly enriched in gene sets. Subsequently, we performed gene expression correlation analysis between these targets and FTO in TCGA HCC cohorts. We could not identify gene targets among the upregulated genes having a negative correlation with FTO expression (data not shown). We then focused on the downregulated genes, particularly those included in positive regulation of cellular component movement processes, in which the gene count of this process was highest in the downregulated genes (figure 4B). Moreover, this pathway was relevant as we found that FTO KD mediated attenuation of cell migration (online supplemental figure S3B). The correlation between FTO and the

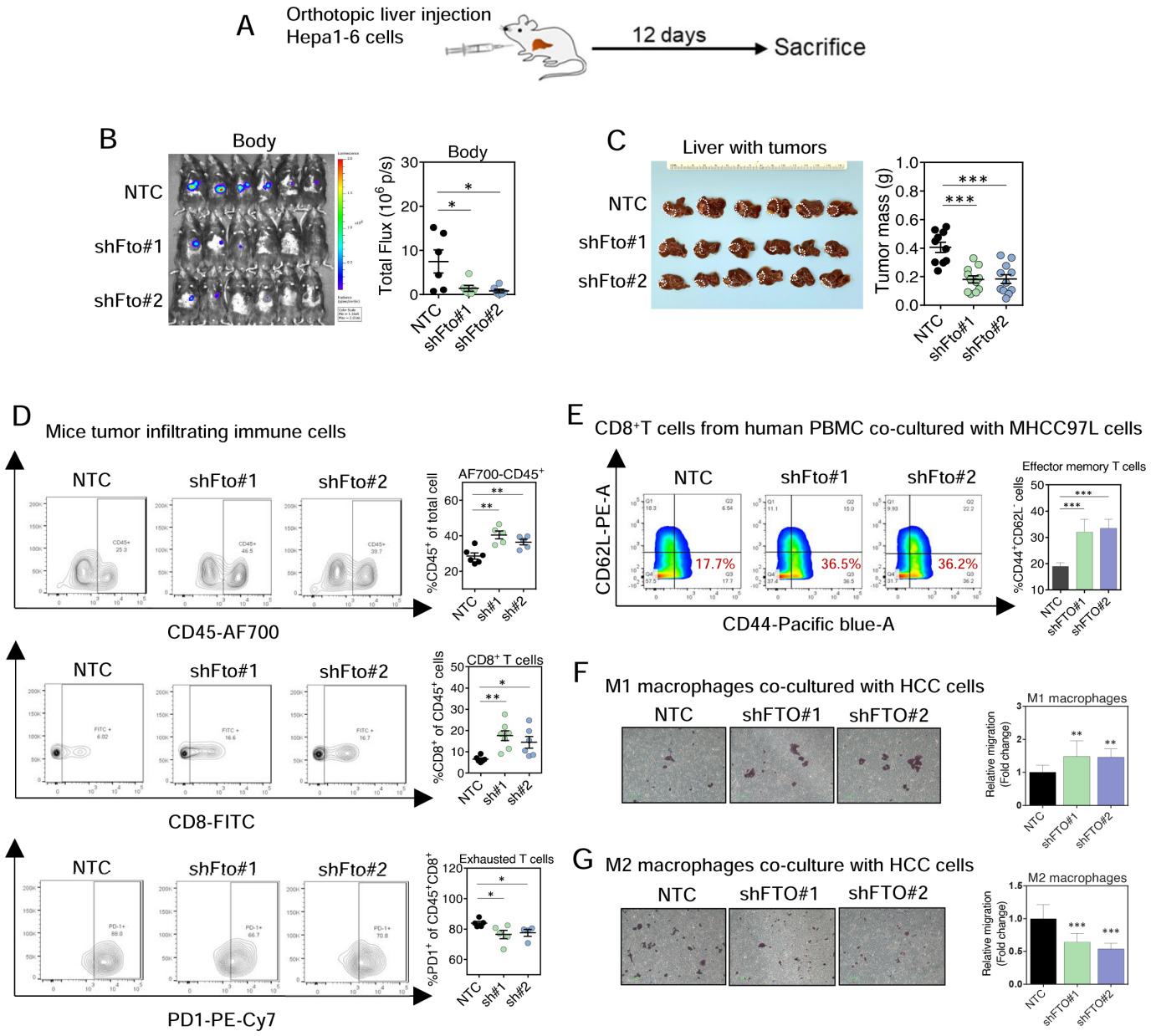

Figure 3 Fat mass and obesity-associated protein (FTO) knockdown (KD) enhanced immune response in vivo and in vitro. (A) Diagram showing orthotopic injection of luciferase-labelled Hepa1-6 cells (non- target control (NTC), shFto#1 and shFto#2) in C57BL/6 mice. (B) Bioluminescent images and quantification of their bioluminescent intensities. (n=6 in each group) (C) Livers with tumours and tumour mass. (D) Proportions of tumour infiltrating immune cells, $CD45^+$, $CD45^+CD8^+$ and $CD45^+CD8^+PD\text{-}1^+$ cells, by flow cytometry. (E) Flow cytometry showing significant increase in $CD44^+CD62L^-$ effector memory $CD8^+$T cells in human peripheral blood mononuclear cells (PBMCs) on coculturing with FTO KD hepatocellular carcinoma (HCC) cells. (F), (G) Migrated M1 and M2 macrophages after coculturing with HCC cells (NTC, shFTO#1 and shFTO#2). (E)-(G) Results were from three independent experiments. One-way analysis of variance followed by Dunnett comparison test, mean±SD, *p<0.05, **p<0.01, ***p<0.001.

potential target genes involved in the process were analysed, and the expression of these genes was also examined in the TCGA HCC cohort. Five potential downstream target genes of FTO were selected for further investigation. To this end, FTO KD significantly downregulated the expression of three potential downstream target genes (GPNMB, PDGFB and ROBO4) in both HepG2 (figure 4C) and 97L (figure 4D) cells.

To determine if the oncogenic effects of FTO depended on its m6A demethylase activity, we established stable FTO-wildtype (FTO-WT) and FTO-mutated (FTO-MUT)-overexpressing PLC cells (online supplemental figure S3C). The FTO-MUT had the mutation at the 316 site of the FTO protein amino acid sequence, with replacement of arginine (R) by alanine (A), hence losing its demethylase activity.[13] Stable overexpression of FTO-WT upregulated the mRNA levels of GPNMB in PLC cells as compared with the empty vector control, while this promoting effect was abolished on FTO mutation (figure 4E).

m6A-Seq was conducted on the mRNA samples isolated from FTO KD or NTC 97L cells to map the m6A modification. The data showed that the vast majority of m6A peaks were distributed in the coding sequence and 3′ UTR regions (figure 4F). FTO KD induced an obvious increase of m6A peaks (figure 4G). The consensus motifs of m6A peaks were identified in the peak region (online supplemental figure S3D). An analysis of the m6A

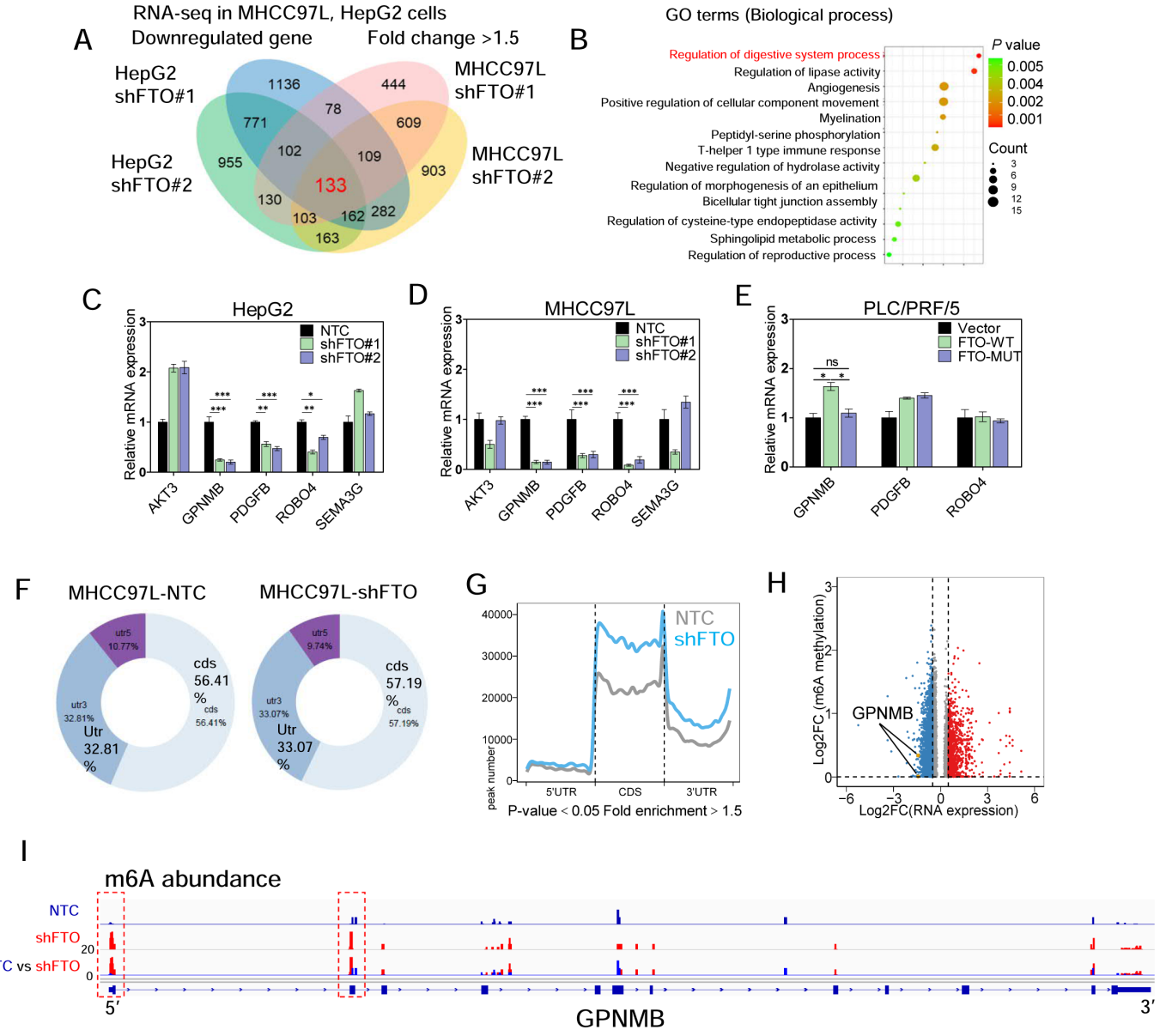

Figure 4 RNA-sequencing and m6A-methylated RNA immunoprecipitation assay identified glycoprotein non-metastatic melanoma protein B (GPNMB) as a downstream target of fat mass and obesity-associated protein (FTO)-mediated N^6-methyadenosine (m6A) modification. (A) Venn diagram and (B) GO biological processes annotation analysis showing genes downregulated by >1.5-fold on FTO knockdown (KD) in HepG2 and 97L cells. (C and D) FTO KD significantly downregulated the mRNA level of potential downstream target genes (GPNMB, PDGFB and ROBO4) in 97L and HepG2 cells, respectively (n=3). (E) FTO- wildtype (FTO-WT) overexpression in PLC cells upregulated the mRNA levels of the three genes but this upregulation was abolished on FTO mutation (n=3) only for GPNMB. (F) Distribution of m6A peaks in different regions of mRNA as detected in m6A-seq assays conducted in control or FTO KD 97L cells. (G) The significantly increased (blue) m6A peaks on FTO KD in 97L cells. (H) The increased m6A abundance of mRNA in upregulated (red) or downregulated (blue) genes on FTO KD in 97L cells. (I) The m6A abundance in the GPNMB transcript. The m6A peaks were called by exome-Peak. t-test, mean±SD, *p<0.05, **p<0.01, ***p<0.001. FTO-MUT, FTO mutated; NTC, non-target control.

modification on GPNMB mRNA on silencing FTO in 97L cells revealed an obvious increase in m6A abundance (figure 4H,I). This is in line with the aforementioned finding that FTO KD significantly decreased the mRNA level of GPNMB (figure 4D). In summary, GPNMB was identified as a direct target of m6A modification.

FTO KD reduced GPNMB mRNA stability via an m6A-YTH N^6-methyladenosine RNA binding protein F2-dependent pathway

According to TCGA database, GPNMB is highly expressed in HCC tumours as well as a number of other cancers (online supplemental figure S4A). GPNMB was found to be significantly upregulated in HCC tumours in both our in-house RNA-seq database with 41 pairs of HCC samples and the TCGA database with 375 HCC patients' samples (figure 5A, left and right panels). GPNMB mRNA expression also showed a positive correlation with FTO expression in TCGA HCC cohort (online supplemental figure S4B). Moreover, silencing FTO significantly downregulated the mRNA and protein levels of GPNMB in 97L cells (figure 5B). Strikingly, FTO KD resulted in global increase in m6A abundance in HCC cells (figure 5C). These findings suggest the link between FTO and GPNMB expression in HCC, with FTO

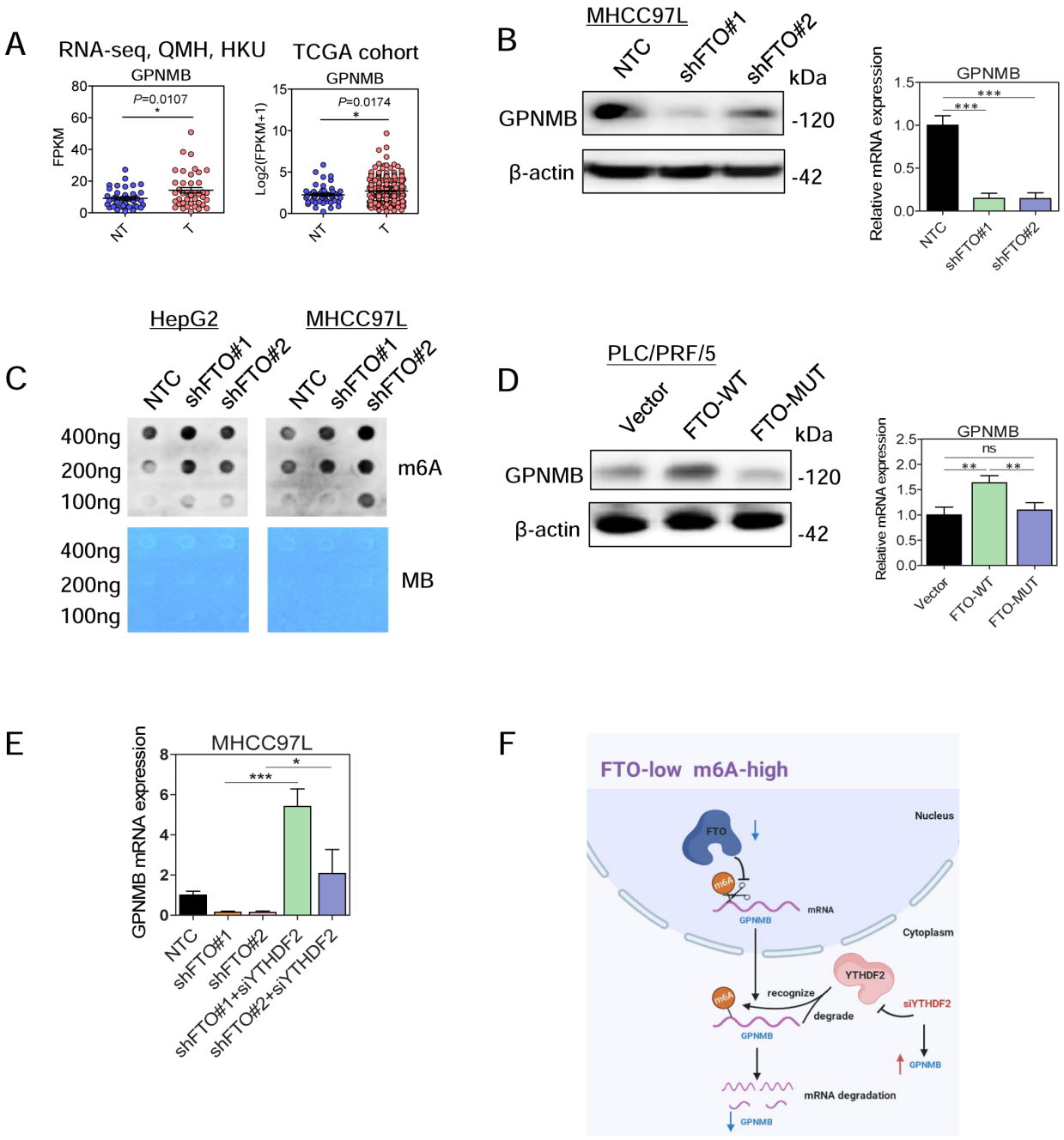

Figure 5 FTO KD attenuated GPNMB mRNA stability through YTHDF2. (A) GPNMB was frequently upregulated in our in-house RNA-seq HCC cohort (n=41 pairs) and TCGA HCC cohort (n=375). (B) The mRNA and protein levels of GPNMB were reduced in FTO stable KD 97L cells. (C) Determination of m6A abundance by Dot Blot assay in HepG2 and 97L cells on FTO stable KD. (D) The mRNA and protein level of GPNMB in PLC cells on overexpression of FTO-WT or FTO-MUT. (E) The mRNA levels of GPNMB in FTO KD 97L cells with or without silencing YTHDF2. (n=3). (F) A schematic diagram illustrating GPNMB expression was regulated by FTO-mediated m6A modification through YTHDF2-mediated mRNA degradation. t-test, mean±SD, *p<0.05, **p<0.01, ***p<0.001). FTO, fat mass and obesity-associated protein; FTO-MUT, FTO mutated; FTO-WT, FTO-wildtype; GPNMP, glycoprotein non-metastatic melanoma protein B; HCC, hepatocellular carcinoma; HKU, University of Hong Kong; QMH, Queen Mary Hospital; qPCR, quantitative PCR; m6A, N^6-methyladenosine; NTC, non-target control; NT, non-tumour; TCGA, The Cancer Genome Atlas; YTHDF2, YTH N^6-methyladenosine RNA binding protein F2.

KD leading to downregulation of GPNMB expression and an increase in m6A abundance.

Next, we confirmed that FTO expression affected GPNMB expression through an m6A-dependent mechanism. To this end, overexpression of FTO-WT increased the mRNA and protein levels of GPNMB as compared with the empty vector control in PLC cells, but this effect was abolished with expression of FTO-MUT (figure 5D). In the in vivo limiting dilution assay to test tumour initiation ability, overexpression of FTO-WT increased the tumour incidence on injection of both 2×10^3 and 2×10^4 HCC cells. In addition, the tumour size was larger in the FTO-WT group with the injection of 2×10^5 cells (online supplemental figure S4C). For the FTO-MUT group, the tumour incidence was reduced with the injection of 2×10^3 cells and unchanged with the injection of 2×10^4 and 2×10^5 cells. The estimated tumour initiation frequency showed a significant increase in

the FTO-WT group when compared with the FTO-MUT group ($p<0.001$) (online supplemental figure S4D), suggesting that the tumourigenesis-promoting properties of FTO likely depend on its m6A demethylase activity.

Previous studies had shown that YTH N^6-methyladenosine RNA binding protein F2 (YTHDF2) selectively binds to m6A-containing mRNA and degrades it.[14] To investigate this, we knocked down YTHDF2 in 97L cells using small interfering RNA specifically targeting YTHDF2 (online supplemental figure S4E). YTHDF2 KD remarkably rescued the downregulation of GPNMB mRNA induced by silencing FTO (figure 5E). The finding suggests that the potential downstream target of FTO, GPNMB, has m6A modification by FTO but is also subjected to YTHDF2-dependent mRNA degradation. This adds another layer of complexity to the regulation of GPNMB expression and highlights the interplay between FTO and YTHDF2 in controlling the stability of GPNMB in HCC (figure 5F).

GPNMB KD inhibited the pro-oncogenic phenotype of HCC

To investigate the role of GPNMB as a potential downstream target of FTO in HCC, stable KD of GPNMB was established in 97L and HepG2 cells using two independent shRNA sequences. Successful KD at the protein level was confirmed in both cell lines (online supplemental figure S5A,B). Silencing GPNMB significantly inhibited cell proliferation (figure 6A) and migration (figure 6B) in both cells. We also assessed the tumour growth in vivo using an orthotopic injection model with luciferase-labelled 97L cells with or without GPNMB KD. GPNMB KD exerted a significant reduction in the tumour-forming ability in the liver (online supplemental figure S5C,D; figure 6C) and resulted in a lower incidence of lung metastasis (figure 6D). These findings indicate that GPNMB plays a crucial role in promoting HCC tumour growth and metastasis, further supporting its role as a downstream target of FTO in HCC. Furthermore, GPNMB KD significantly suppressed the colony formation and sphere formation abilities in 97L and HepG2 cells (figure 6E,F). To further assess the tumour-initiating ability of GPNMB KD cells in vivo, a limiting dilution assay, in which varying numbers of HCC cells (2×10^5, 2×10^4 and 2×10^3) were subcutaneously injected into nude mice, showed a significantly lower tumour-initiating capacity in shGPNMB cells compared with NTC cells (figure 6G). Extreme limiting dilution analysis on the limiting dilution assay showed a 3.6-fold reduction in 'stem-cell frequency' ($p=8.94\times10^{-4}$), which estimates the frequency of self-renewing tumour-initiating cells (figure 6H). Taken together, these results confirm the functional roles of GPNMB in promoting HCC tumour initiation, growth and metastasis.

GPNMB activated AKT, ERK and WNT pathways to promote HCC progression

To further investigate the underlying mechanism of GPNMB in HCC progression, we overexpressed GPNMB in FTO KD 97L cells (online supplemental figure S6A). GPNMB overexpression significantly rescued the suppressed abilities of cell proliferation (figure 7A), migration (figure 7B, online supplemental figure S6B), sphere formation (figure 7C, online supplemental figure S6C) in FTO KD 97L cells. Previous studies have shown that GPNMB signalling increases the phosphorylation of ERK and AKT in different models and cell types,[15–17] as well as activates the canonical WNT pathway, as evidenced by increased β-catenin transcriptional activity in breast cancer cells.[18 19] Therefore, we examined the activation of WNT, AKT and ERK pathways. GPNMB KD downregulated the expression of β-catenin, phosphorylated AKT and phosphorylated ERK in 97L cells (figure 7D, online supplemental figure S6D), while GPNMB overexpression in the FTO KD 97L cells abrogated these effects (figure 7E, online supplemental figure S6E). These findings suggest that GPNMB may promote HCC progression through the activation of WNT, AKT and ERK signalling pathways.

GPNMB was packaged into sEVs derived from HCC cells and suppressed immune cell activation

Previous studies showed that GPNMB could be packaged into sEVs of mouse melanoma cells.[20] In this study, we showed that GPNMB was also packaged into sEVs produced by HCC cells (figure 7F; online supplemental figure S6G). Of note, we found presence and also upregulation of GPNMB in sEVs of HCC patients' plasma when compared with those from healthy subjects (online supplemental figure S6F). Next, we extracted sEVs from FTO-overexpressing (FTO-WT or FTO-MUT (R316A)) PLC and 97L cells with GPNMB KD. We found that sEVs derived from the FTO-WT-overexpressing HCC cells contained high levels of GPNMB protein, whereas those from the FTO-MUT-overexpressing HCC cells had GPNMB protein levels only comparable to the control group (figure 7F and online supplemental figure S6G). Furthermore, sEVs derived from GPNMB KD HCC cells showed a much lower level of GPNMB protein compared with the NTC group (figure 7F and online supplemental figure S6G). Additionally, nanoparticle tracking analysis identified the sEVs derived from HCC cell lines had a size peak around 120–140 nm (online supplemental figure S6H). Transmission electron microscopy confirmed that the sEVs had a cup-shaped morphology and a diameter of around 30–160 nm. We next examined whether GPNMB was localised within sEVs or present on the surface of sEVs. First, our immunogold labelling indicated that GPNMB was present on the membrane of sEVs (figure 7G). Then, we treated sEVs from 97L with proteinase K to degrade proteins at a concentration that led to the degradation of the outer membrane proteins such as CD63, but not the intravesicular HSP70 (figure 7H). The findings showed that the distribution of GPNMB was limited to the sEV surface. These findings suggest that GPNMB is present on the surface of sEVs derived from HCC cells.

sEV-GPNMB from HCC cells bound to SDC4 on $CD8^+$ T cells and suppressed activation of $CD8^+$ T cells

We questioned how FTO regulated GPNMB to affect immune microenvironment. Our previous single-cell RNA sequencing study on HCC patients' tumours[12] revealed that the expression of GPNMB negatively correlated with the fraction of $CD8^+$ T cells ($p=0.015$, $r=-0.85$) (figure 7I). To address the relationship of GPNMB, sEVs and $CD8^+$ T cells, HCC-cell derived sEVs were added to $CD8^+$ T cells isolated from PBMC of healthy subjects. A significant reduction of $CD44^+CD62L^-$ effector memory T cell proportion was observed in sEVs-NTC treated $CD8^+$ T cells, as compared with PBS control (figure 7J). In contrast, this suppressive effect on $CD8^+$ T cells was abrogated by sEVs from shGPNMB HCC cells (figure 7J and online supplemental figure S6I). Our finding suggests that GPNMB may inhibit the activation of $CD8^+$ T cells via its packaging into sEVs.

Next, we examined whether GPNMB located on the surface of sEVs could bind to SDC4, which is a receptor protein of $CD8^+$ T cells. To this end, we overexpressed a fusion protein, GFP-GPNMB, in 97L cells, and used the sEVs derived from GFP-GPNMB-overexpressing cells to treat $CD8^+$ T cells ($n=4\times10^5$) isolated from the PBMCs of healthy subjects at a

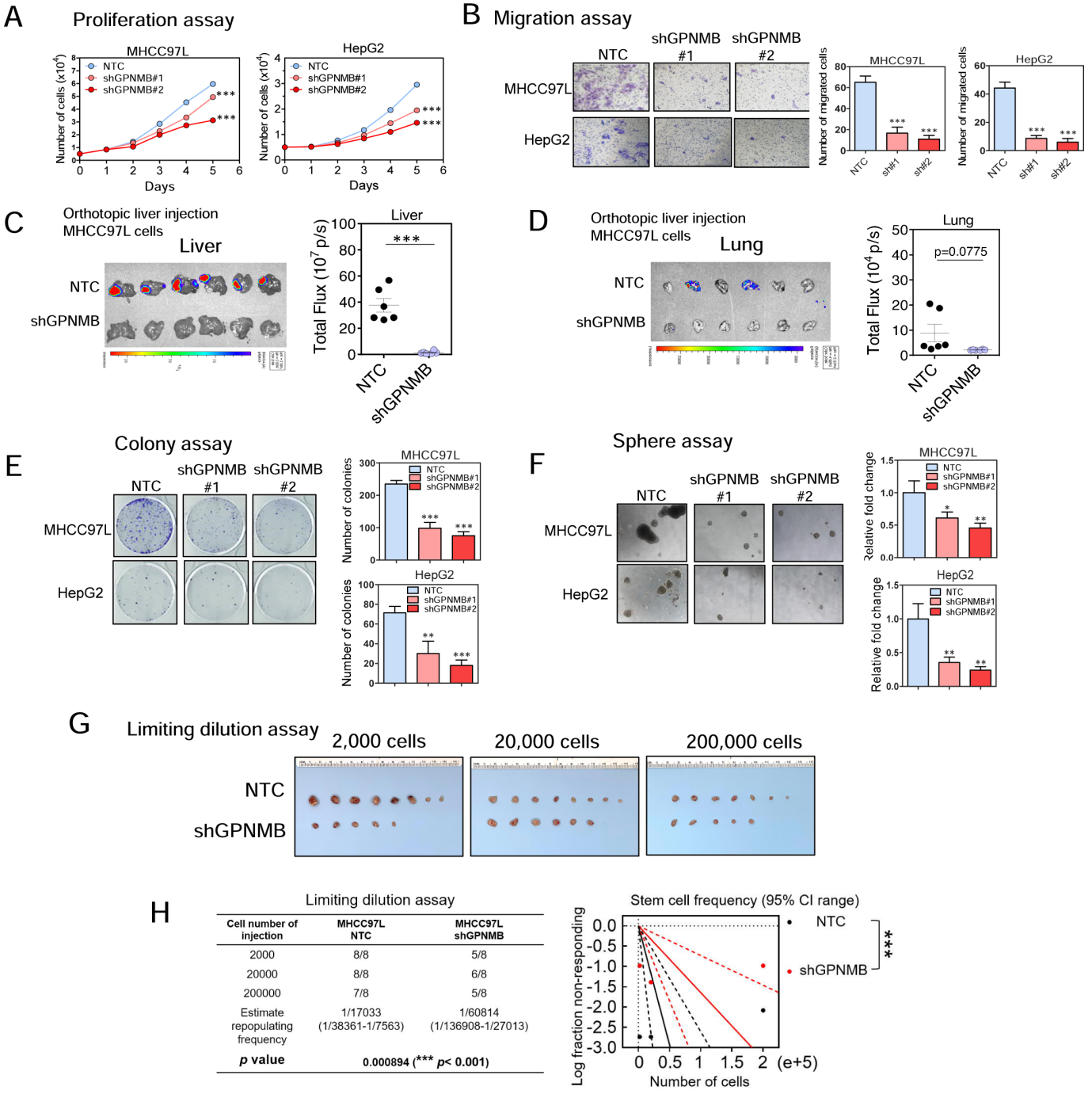

Cell number of injection	MHCC97L NTC	MHCC97L shGPNMB
2000	8/8	5/8
20000	8/8	6/8
200000	7/8	5/8
Estimate repopulating frequency	1/17033 (1/38361-1/7563)	1/60814 (1/136908-1/27013)
p value	0.000894 (*** *p*< 0.001)	

Figure 6 Glycoprotein non-metastatic melanoma protein B (GPNMB) knockdown (KD) inhibited hepatocellular carcinoma tumour growth metastasis and stemness. (A) GPNMB KD significantly inhibited proliferation of HepG2 and 97L cells. (B) The numbers of migrated cells were significantly reduced on fat mass and obesity-associated protein KD (n=3). (C and D) Orthotopic liver injection with Hepa1-6 with or without GPNMB KD in nude mice. Bioluminescence images of livers and lungs, with quantification of their bioluminescent intensities. (E) KD of GPNMB significantly suppressed the colony formation ability in 97L and HepG2 cells (n=3). (F) KD of GPNMB significantly reduced the size and number of hepatospheres formed by 97L and HepG2 cells (n=3). (G and H) Limiting dilution assay to assess the effects of GPNMB KD on tumourigenicity in nude mice. 2×10^3, 2×10^4 and 2×10^5 97 L cells were injected subcutaneously into nude mice. The tumour incidence rate for each group was recorded at the end of the experiments. Tumour initiating capacity was calculated by the CIs with the formula of CI=1/(stem cell frequency). t-test, mean±SD, *p<0.05, **p<0.01, ***p<0.001. NTC, non-target control.

final concentration of 20 µg/mL for 16 hours. SDC4 expression was detected in the protein complexes pulled down by the GFP antibody (figure 7K).

To investigate whether GPNMB located on the surface of sEVs inhibited $CD8^+$ T cell activation through binding to SDC4, we pre-treated $CD8^+$ T cells with a mouse IgG antibody or neutralising antibody (NA)[21 22] against SDC4 ectodomain for 2 hours, followed by treatment with the sEVs derived from 97L-NTC cells, the NA of SDC4 significantly enhanced the activation of $CD8^+$ T cells as compared with the IgG control group (figure 7L and online supplemental figure S6J). Taken altogether, the results showed

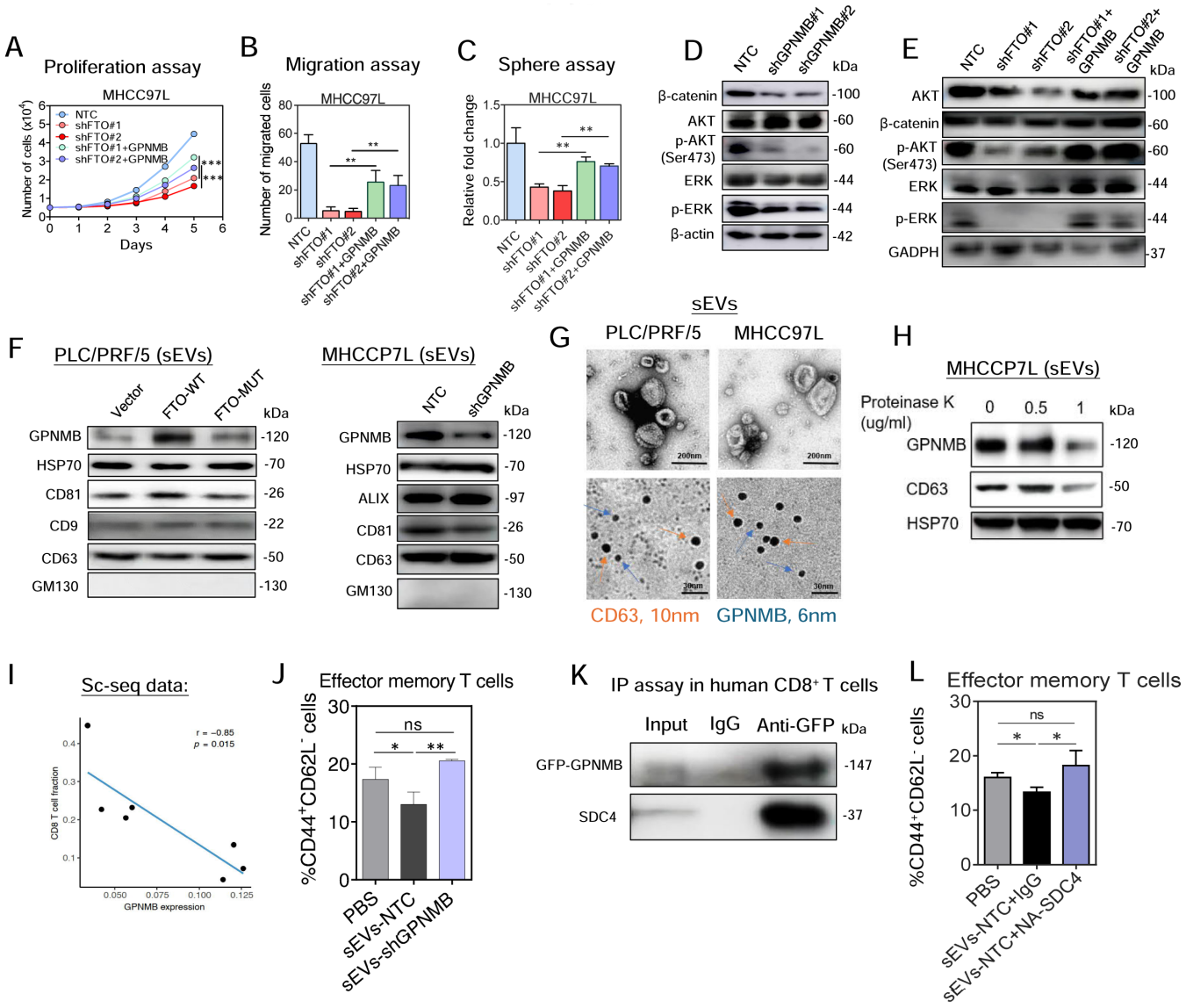

Figure 7 Fat mass and obesity-associated protein (FTO) activated AKT, ERK and WNT pathways and suppressed immune cell activation through upregulating glycoprotein non-metastatic melanoma protein B (GPNMB). (A) The cell proliferation, (B) migratory ability and (C) sphere forming ability on rescue of FTO knock down (KD) with overexpression of GPNMB in 97 L cells (n=3). (D) Western blotting showing GPNMB KD suppressed activation of AKT, ERK, WNT signalling pathway in 97L cells. (E) Overexpression of GPNMB rescued the activation of AKT, ERK, WNT signalling pathways shown with western blotting in 97L cells. (F) Western blots showing presence of GPNMB in small extracellular vesicles (sEVs) derived from PLC (EV, FTO-wildtype (FTO-WT), FTO-mutated (FTO-MUT)) and 97L cells (non-target control (NTC), shGPNMB). CD63, CD81, HSP70, CD9, CD63 and ALIX are positive EV markers and GM130 is a negative EV marker, and they were used as loading control. (G) Representative electron micrographs showing the morphology of sEVs from PLC and 97L cells (upper panel) (scale bar=200 nm), and immunogold labelling (lower panel) (scale bar=30 nm). (H) Western blot showing the protein expression of GPNMB, surface-sEVs marker CD63 and intra-sEV marker HSP70 in 97L-derived sEVs treated with increasing concentrations of proteinase K. (I) The correlation between GPNMB expression and $CD8^+$ T cell fraction was confirmed in Sc-seq data of hepatocellular carcinoma patients. (J) Flow cytometry showing significant increase $CD44^+CD62L^-$ effector memory T cells on treating with sEVs derived from GPNMB KD 97L cells compared with NTC group. (K) Co-immunoprecipitation assay showing GFP-GPNMB located on the surface of sEVs interacted with SDC4 as a surface receptor on human $CD8^+$ T cells. Total cell lysate (input) was used as positive control. (L) Flow cytometry showing significant increase $CD44^+CD62L^-$ effector memory T cells on treating with SDC4 blocking antibody. t-test, mean±SD, **p<0.01, ***p<0.001.

that GPNMB inhibited $CD8^+$ T cell activation by directly binding to SDC4 via sEVs.

Blockade of FTO sensitised HCC to anti-PD-1 immune checkpoint blockade therapy

We employed three mouse models to examine the effects of targeting FTO. In an orthotopic liver injection mouse model, pharmacological inhibition of FTO by its specific inhibitor CS2 suppressed tumour growth and enhanced the antitumour efficiency of tyrosine kinase inhibitor, Sorafenib, in combination treatment (online supplemental figure S7A,B). CS2 treatment significantly downregulated the protein expression of GPNMB, phosphorylated AKT and phosphorylated ERK (online supplemental figure S7C). On the other hand, CS2 alone or combined with anti-PD-1 also significantly increased the infiltration of $CD45^+$ $F4/80^+$ macrophages and antitumoural M1 macrophages

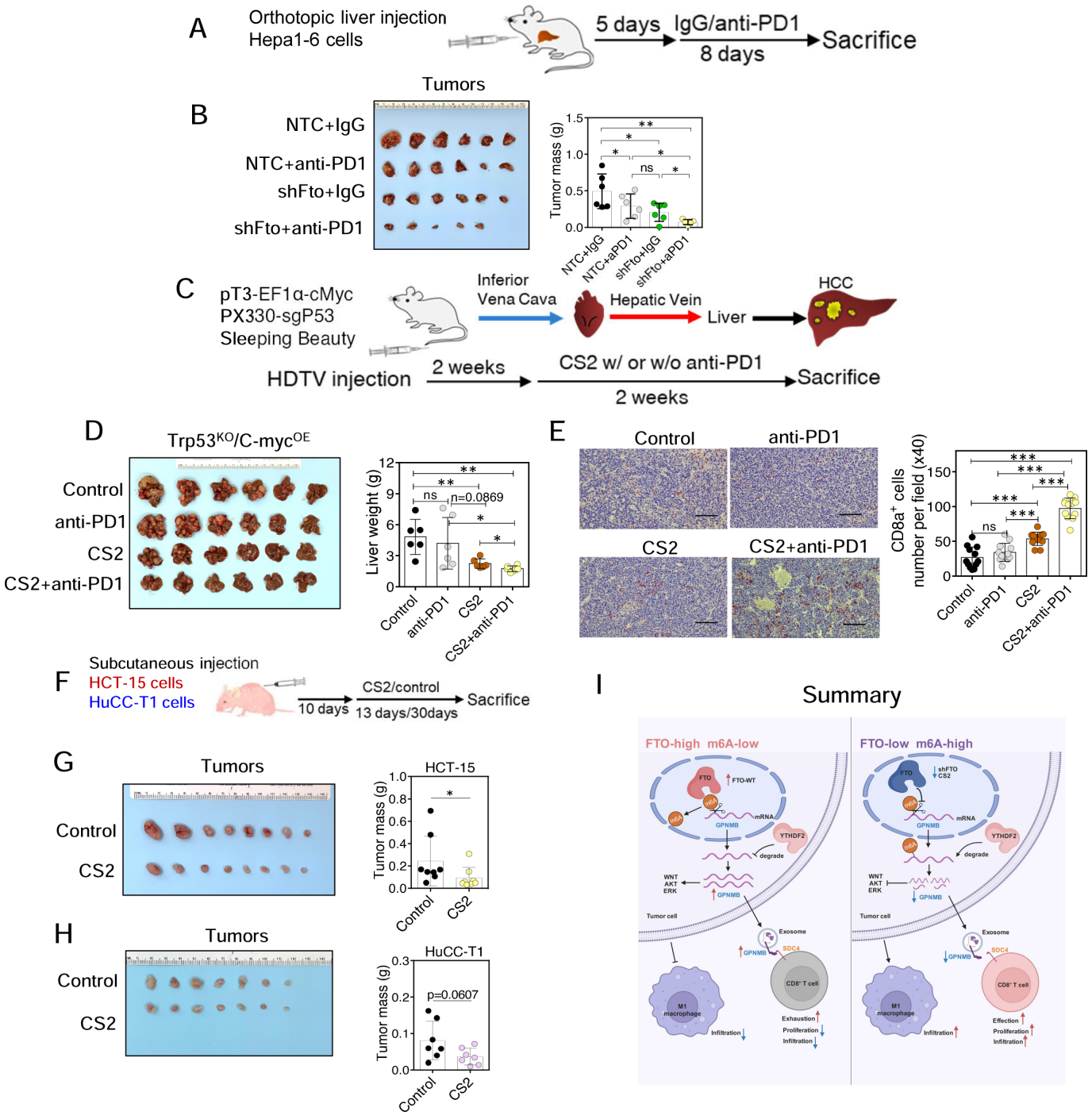

Figure 8 Blockade of fat mass and obesity-associated protein (FTO) sensitised hepatocellular carcinoma to anti-PD-1 immune checkpoint blockade therapy. (A) Schematic diagram illustrating the workflow of anti-PD-1 treatment in orthotopic liver injection mouse model with Hepa1-6 cells injection (non-target control (NTC)/shFto+IgG, NTC/shFto+anti-PD-1). (B) Tumours dissected from livers and their tumour masses. (C) A schematic summary of FTO inhibitor CS2 and anti-PD-1 treatment in hydrodynamic tail vein injection (p53 KO/c-Myc) model with induced tumours in mice. (D) Livers with tumours and liver weights representing the tumour masses on treatment with anti-PD-1, CS2 and CS2+anti-PD-1 combination treatment. (E) Immunohistochemical staining of tumour infiltrating $CD8^+$ T cells in liver tumour tissues of mice (left panel) (scale bar=100 µm) and quantification (right panel). (F) A summary of FTO inhibitor treatment in human colorectal adenocarcinoma HCT-15 cells and human cholangiocarcinoma HuCCT1 cell-derived subcutaneous xenografts. (G and H) Tumour xenografts of HCT-15 and HuCCT1 cells treated with vehicle control and CS2. (I) A schematic summary of this study. t-test, mean±SD, *p<0.05, **p<0.01.

($CD45^+$ $F4/80^+$ $CD86^+$), when compared with control group (online supplemental figure S7D). Since silencing FTO expanded $CD8^+$ T cell infiltration and effector memory $CD8^+$ T cell activation (figure 3D,E), we evaluated the potential enhancing effect of targeting FTO using genetic silencing and immune checkpoint blockade (ICB) with an immune checkpoint inhibitor anti-PD-1 in an orthotopic liver injection mouse model, in which mouse hepatoma Hepa1-6 cells with or without FTO KD were injected (figure 8A). The combination treatment of anti-PD-1 and FTO KD showed the most significant tumour growth

suppression (figure 8B). Finally, a hydrodynamic tail-vein injection (HDTVi) model was employed to induce spontaneous HCC tumours in C57BL/6 mice with CRISPR/Cas9-mediated loss-of-function genome editing of endogenous TP53 and Sleeping Beauty transposon-driven C-Myc overexpression (Trp53KO/C-MycOE) (figure 8C). Anti-PD-1 alone failed to impede tumour development, consistent with previous findings.[23] In contrast, targeting FTO pharmacologically with CS2 alone significantly decreased the tumour masses, and the combination of CS2-anti-PD-1 resulted in further significant reduction of tumour masses (figure 8D). These findings suggest that targeting FTO, either by pharmacological inhibition or genetic silencing, suppresses tumour growth and enhances the therapeutic effects of immune checkpoint blockade with anti-PD-1 and Sorafenib in HCC mouse models.

Immunohistochemistry on the HDTVi mouse tumour tissues revealed that the number of tumour-infiltrating $CD8^+$ T cells was remarkably increased in the CS2-anti-PD-1 combination group compared with either the CS2 or anti-PD-1 single treatment group (figure 8E). Furthermore, depletion of $CD8^+$ T cells using anti-CD8 antibody in immunocompetent mice abrogated the tumour-suppressive effect of CS2 and CS2/anti-PD-1 combo (online supplemental figure S8A–C). As CS2 is a specific inhibitor of FTO demethylase, these findings suggest that FTO/m6A promotes HCC progression through the activation of AKT and ERK signalling pathways.

Additionally, we tested the therapeutic efficiency of the FTO inhibitor CS2 in two other cancer cell lines with high FTO expression levels: HCT-15 (human colorectal adenocarcinoma) and HuCC-T1 (human cholangiocarcinoma), based on TCGA data (online supplemental figure S1A). In a subcutaneous xenograft mouse model, mice were treated with CS2 after tumour formation (figure 8F). CS2 was found to significantly decrease the tumour growth in HCT-15 cells (figure 8G) and a trend in HuCC-T1 cells (figure 8H). Taken together, the findings suggest that targeting FTO with CS2 may be a promising treatment strategy for HCC and possibly for some other cancer types. Moreover, it may potentially sensitise HCC to ICB therapy.

DISCUSSION

This study demonstrates the crucial role of FTO in promoting HCC growth, metastasis and stemness. We also identified GPNMB as a novel downstream target of FTO, which regulated the m6A demethylation of GPNMB mRNA. Importantly, we demonstrated that GPNMB was packaged into sEVs derived from HCC cells and bound to the surface receptor SDC4 of $CD8^+$ T cells, resulting in the inhibition of $CD8^+$ T cell activation (figure 8I).

In this study, our data provides important insights into the role of FTO in regulating the immune response in cancer. We demonstrated that FTO upregulated the protein level of GPNMB in sEVs through its m6A demethylase activity. Furthermore, GPNMB was present and also upregulated in HCC patients' plasma sEVs. Single-cell RNA sequencing study on human HCC tumours revealed that the expression of GPNMB negatively correlated with the fraction of $CD8^+$ T cells. GPNMB on the surface of sEVs was found to inhibit $CD8^+$ T cell activation by directly binding to SDC4, a receptor upregulated on activated T cells and known to enhance T cell activation.[24 25] This GPNMB/SDC4 pathway has been previously reported to inhibit human allogeneic T-cell responses. Additionally, FTO KD was shown to activate immune response by sensitising melanoma cells to anti-PD-1 treatment in mice.[26] A recent study reported that GPNMB showed immune suppression in hepatic parenchymal cells.[27] Our findings in this study not only showed the immune suppressive effect of the FTO/GPNMB axis, but also uncovered the novel finding that sEVs play an important role in mediating the immune suppressive effect by interaction with SDC4 in $CD8^+$ T cells. The sEV-GPNMB may be as a plausible marker of HCC prognosis.

This study demonstrates the potential therapeutic value of CS2, an FTO inhibitor, in suppressing tumour growth and enhancing the effectiveness of existing cancer treatments. CS2 has previously been reported to inhibit dihydroorotate dehydrogenase, block de novo pyrimidine biosynthesis[28] and exhibit potent antileukaemic efficacy in samples with high FTO expression through binding directly to FTO protein.[9] It has also been tested in clinical trials for cancer therapy.[29–32] In this study, CS2 was found to suppress tumour growth and enhance the antitumour efficiency of Sorafenib in a mouse model. Furthermore, the combination of CS2 and anti-PD-1 treatment resulted in a significant reduction in tumour mass compared with single-agent treatment in spontaneous tumourigenesis model. Interestingly, CS2 also decreased tumour mass in human colorectal adenocarcinoma and cholangiocarcinoma cell lines with high FTO expression. Depletion of $CD8^+$ T cells in immunocompetent mice abrogated the tumour-suppressing effect of CS2 and CS2/anti-PD-1 combo, further confirming the immune suppressive effect mediated via interaction with $CD8^+$ T cells. While further systematic studies are needed to confirm the overall anticancer efficacy of CS2 and explore other potential mechanisms of action, these findings suggest that CS2 may have therapeutic potential in different types of cancers with high FTO expression.

In summary, our results demonstrated that targeting the FTO/m6A/GPNMB axis could significantly suppress tumour growth, metastasis, stemness and enhance immune activation, highlighting the broad potential of targeting FTO signalling by effective inhibitors (alone or in combination with other therapeutic agents) for cancer therapy. These insights contribute to the understanding of the molecular mechanisms underlying FTO's role in HCC and provide a foundation for the development of targeted therapeutics against FTO.

Acknowledgements The authors thank the Centre for PanorOmic Sciences Imaging and Flow Cytometry Core at the LKS Faculty of Medicine of The University of Hong Kong for technical assistance and support; the Centre for Comparative Medicine Research of The University of Hong Kong for providing animals, husbandry and facilities for animal experimentation; and the Electron Microscope Unit for providing technical support. Figure 5G and graphical abstract figure were created with Biorender.com.

Contributors AC, VXZ and IO-LN provided the study concept and design. AC, VXZ and IO-LN wrote the manuscript. AC, VXZ, QZ, DW-HH, XL, CMW and IO-LN interpreted and analysed the data. AC, VXZ, KM-FS, LT, HH, XW, EL, JL, MFJL performed the experiments. IO-LN and MFJL collected the patients' samples. LT and XW advised on extracellular vesicle-related experiments. IO-LN provided financial support. IO-LN is responsible for the overall content as the guarantor and supervised the project. All authors approved the final version of the manuscript.

Funding This project was supported in part by grants from the Research Grants Council of Hong Kong—Theme-based Research Scheme (T12-716/22R), Innovation and Technology Commission grant of Hong Kong SAR Government to State Key Laboratory of Liver Research (ITC PD/17-9), National Natural Science Foundation of China (82394451) and University Development Fund of The University of Hong Kong. IOLN is Loke Yew Professor in Pathology. AC is a Hong Kong Scholar.

Competing interests None declared.

Patient and public involvement Patients and/or the public were not involved in the design, or conduct, or reporting, or dissemination plans of this research.

Patient consent for publication Not applicable.

Ethics approval All experimental procedures on mice were approved by the Committee on the Use of Live Animals in Teaching and Research of the University of

Hong Kong (CULATR 5089-19 and 5688-21) and conducted in accordance with the Animals (Control of Experiments) Ordinance of Hong Kong.

Provenance and peer review Not commissioned; externally peer reviewed.

Data availability statement All data relevant to the study are included in the article or uploaded as supplementary information.

ORCID iDs
Ao Chen http://orcid.org/0000-0002-2330-0650
Chun Ming Wong http://orcid.org/0000-0002-2497-7858
Irene Oi-Lin Ng http://orcid.org/0000-0001-7532-2029

REFERENCES

1 Meyer KD, Saletore Y, Zumbo P, *et al*. Comprehensive analysis of mRNA methylation reveals enrichment in 3′ UTRs and near stop codons. *Cell* 2012;149:1635–46.
2 Frye M, Harada BT, Behm M, *et al*. RNA modifications modulate gene expression during development. *Science* 2018;361:1346–9.
3 Shi H, Wei J, He C. Where, when, and how: context-dependent functions of RNA methylation writers, readers, and erasers. *Mol Cell* 2019;74:640–50.
4 Yang Y, Hsu PJ, Chen Y-S, *et al*. Dynamic transcriptomic M6A decoration: writers, erasers, readers and functions in RNA metabolism. *Cell Res* 2018;28:616–24.
5 Zhao BS, Roundtree IA, He C. Post-transcriptional gene regulation by mRNA modifications. *Nat Rev Mol Cell Biol* 2017;18:31–42.
6 Liu N, Dai Q, Zheng G, *et al*. N 6-Methyladenosine-dependent RNA structural switches regulate RNA–protein interactions. *Nature* 2015;518:560–4.
7 Jia G, Fu Y, Zhao X, *et al*. N 6-Methyladenosine in nuclear RNA is a major substrate of the obesity-associated FTO. *Nat Chem Biol* 2011;7:885–7.
8 Wang J-Y, Chen L-J, Qiang P. The potential role of N6-Methyladenosine (M6A) demethylase fat mass and obesity-associated gene (FTO) in human cancers. *Onco Targets Ther* 2020;13:12845–56.
9 Su R, Dong L, Li Y, *et al*. Targeting FTO suppresses cancer stem cell maintenance and immune evasion. *Cancer Cell* 2020;38:79–96.
10 Li J, Zhu L, Shi Y, *et al*. m6A demethylase FTO promotes hepatocellular carcinoma tumorigenesis via mediating PKM2 demethylation. *Am J Transl Res* 2019;11:6084–92.
11 Zhao Y, You S, Yu Y-Q, *et al*. Decreased nuclear expression of FTO in human primary hepatocellular carcinoma is associated with poor prognosis. *Int J Clin Exp Pathol* 2019;12:3376–83.
12 Ho DW-H, Tsui Y-M, Chan L-K, *et al*. Single-cell RNA sequencing shows the immunosuppressive landscape and tumor heterogeneity of HBV-associated hepatocellular carcinoma. *Nat Commun* 2021;12:3684.
13 Chen A, Chen X, Cheng S, *et al*. FTO promotes SREBP1C maturation and enhances CIDEC transcription during lipid accumulation in HEPG2 cells. *Biochimica et Biophysica Acta (BBA) - Molecular and Cell Biology of Lipids* 2018;1863:538–48.
14 Wang X, Lu Z, Gomez A, *et al*. N6-Methyladenosine-dependent regulation of messenger RNA stability. *Nature* 2014;505:117–20.
15 Maric G, Rose AA, Annis MG, *et al*. Glycoprotein non-metastatic B (GPNMB): a metastatic mediator and emerging therapeutic target in cancer. *Onco Targets Ther* 2013;6:839–52.
16 Nakano Y, Suzuki Y, Takagi T, *et al*. Glycoprotein nonmetastatic melanoma protein B (GPNMB) as a novel neuroprotective factor in cerebral ischemia–reperfusion injury. *Neuroscience* 2014;277:123–31.
17 Saade M, Araujo de Souza G, Scavone C, *et al*. The role of GPNMB in inflammation. *Front Immunol* 2021;12:674739.
18 Maric G, Annis MG, MacDonald PA, *et al*. GPNMB augments Wnt-1 mediated breast tumor initiation and growth by enhancing Pi3K/AKT/mTOR pathway signaling and B-Catenin activity. *Oncogene* 2019;38:5294–307.
19 Liu J, Xiao Q, Xiao J, *et al*. WNT/B-Catenin signalling: function, biological mechanisms, and therapeutic opportunities. *Sig Transduct Target Ther* 2022;7.
20 Tomihari M, Chung J-S, Akiyoshi H, *et al*. DC-HIL/glycoprotein Nmb promotes growth of melanoma in mice by inhibiting the activation of tumor-reactive T cells. *Cancer Res* 2010;70:5778–87.
21 Echtermeyer F, Bertrand J, Dreier R, *et al*. Syndecan-4 regulates ADAMTS-5 activation and cartilage breakdown in osteoarthritis. *Nat Med* 2009;15:1072–6.
22 Polte T, Petzold S, Bertrand J, *et al*. Critical role for Syndecan-4 in dendritic cell migration during development of allergic airway inflammation. *Nat Commun* 2015;6:7554.
23 Chiu D-C, Yuen V-H, Cheu J-S, *et al*. Hepatocellular carcinoma cells up-regulate PVRL1, stabilizing PVR and inhibiting the cytotoxic T-cell response via TIGIT to mediate tumor resistance to PD1 inhibitors in mice. *Gastroenterology* 2020;159:609–23.
24 Teixé T, Nieto-Blanco P, Vilella R, *et al*. Syndecan-2 and-4 expressed on activated primary human CD4+ lymphocytes can regulate T cell activation. *Mol Immunol* 2008;45:2905–19.
25 Harris E, Elmer JJ. Optimization of electroporation and other non-viral gene delivery strategies for T cells. *Biotechnol Prog* 2021;37:e3066.
26 Yang S, Wei J, Cui Y-H, *et al*. M6A mRNA demethylase FTO regulates melanoma tumorigenicity and response to anti-PD-1 blockade. *Nat Commun* 2019;10:2782.
27 Meng Y, Zhao Q, Sang Y, *et al*. GPNMB+ Gal-3+ hepatic parenchymal cells promote immunosuppression and hepatocellular carcinogenesis. *EMBO J* 2023;e114060.
28 Peters GJ, Kraal I, Pinedo HM. In vitro and in vivo studies on the combination of Brequinar sodium (DUP-785; NSC 368390) with 5-fluorouracil; effects of uridine. *Br J Cancer* 1992;65:229–33.
29 de Forni M, Chabot GG, Armand JP, *et al*. Phase I and pharmacokinetic study of Brequinar (DUP 785; NSC 368390) in cancer patients. *Eur J Cancer* 1993;29A:983–8.
30 Burris HA 3rd, Raymond E, Awada A, *et al*. Pharmacokinetic and phase I studies of Brequinar (DUP 785; NSC 368390) in combination with cisplatin in patients with advanced malignancies. *Invest New Drugs* 1998;16:19–27.
31 Noe DA, Rowinsky EK, Shen HS, *et al*. Phase I and pharmacokinetic study of Brequinar sodium (NSC 368390). *Cancer Res* 1990;50:4595–9.
32 Schwartsmann G, Dodion P, Vermorken JB, *et al*. Phase I study of Brequinar sodium (NSC 368390) in patients with solid malignancies. *Cancer Chemother Pharmacol* 1990;25:345–51.

Supplementary Figure 1

A

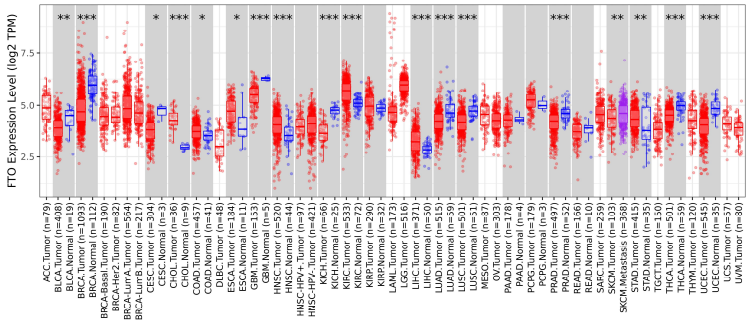

B

The etiology of the patients

Number of patients	Hepatitis B Virus (HBV) Positive	Hepatitis B Virus (HBV) Negative	Not available
41	41	0	0
95	85	6	4

C

DNA Marker	MHCC97L[4]	MHCC97L (L-171218744P)
AMEL	X, Y	X, Y
CSF1PO	11, 13	11, 13
D13S317	8	8
D16S539	12	12
D5S818	12,13	12,13
D7S820	10	10
TH01	9	9
TPOX	8	8
vWA	14	14
D18S51	--	13, 22
D21S11	--	31.2
D3S1358	--	15, 16
D8S1179	--	12, 13
FGA	--	21, 24
Penta D	--	8, 9
Penta E	--	11, 17
Number of shared alleles		12
Total number of alleles in the reference profile		12
Percent match		100%

The tested cell line has 100% match with MHCC97L. Therefore, they are considered to be related from a common ancestry.

D

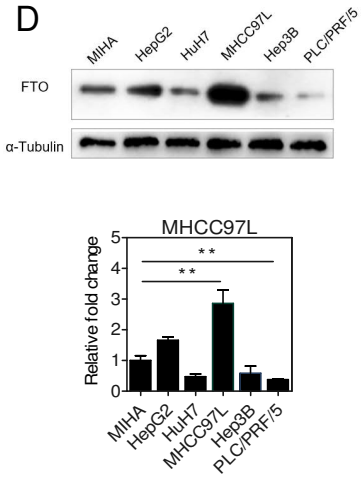

E

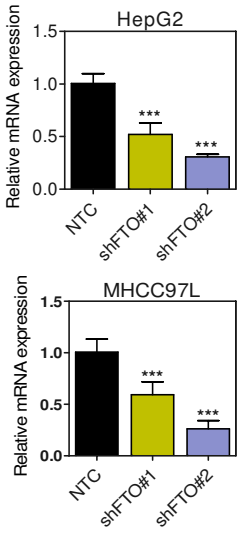

F

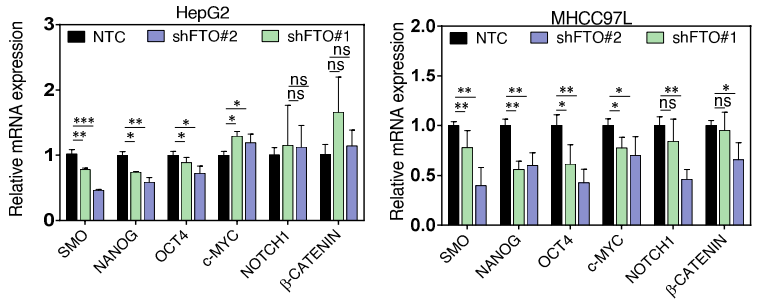

Supplementary Figure 2

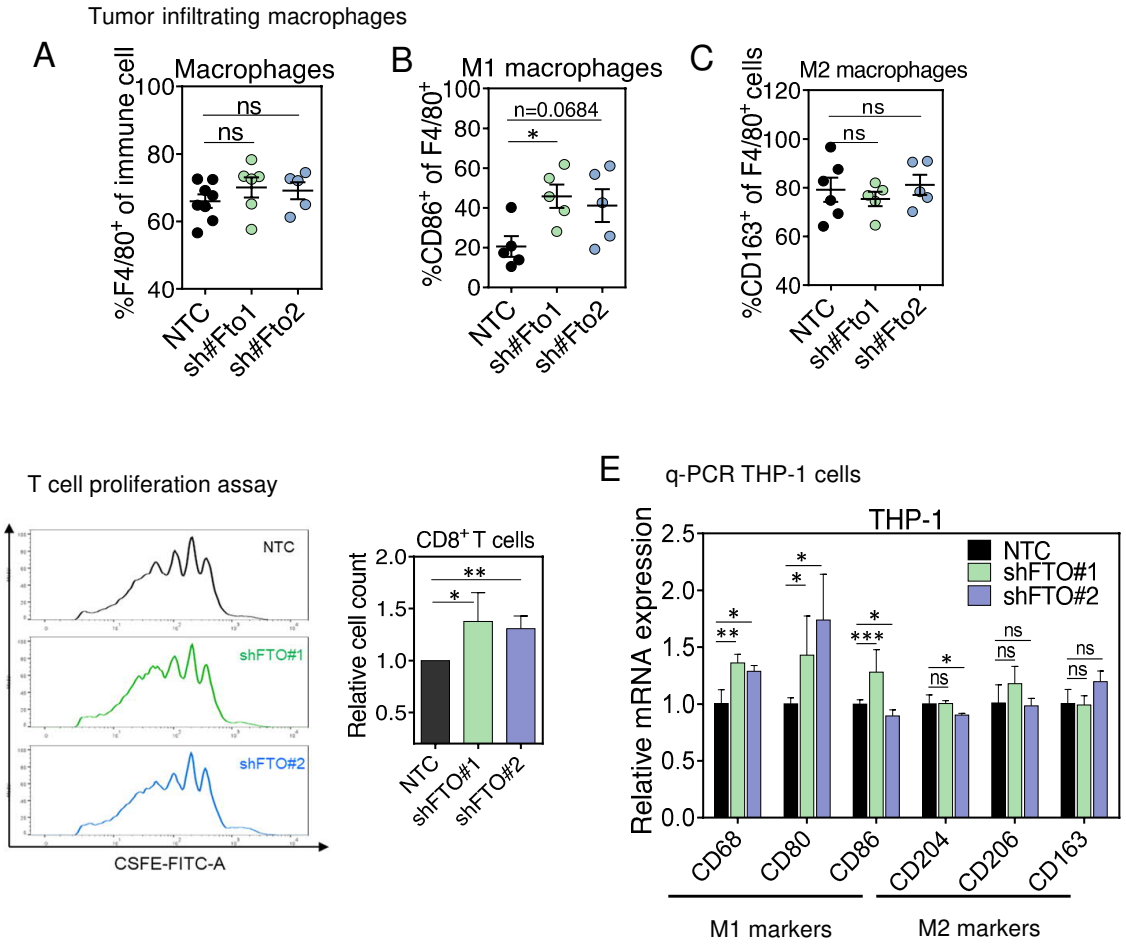

Supplementary Figure 3

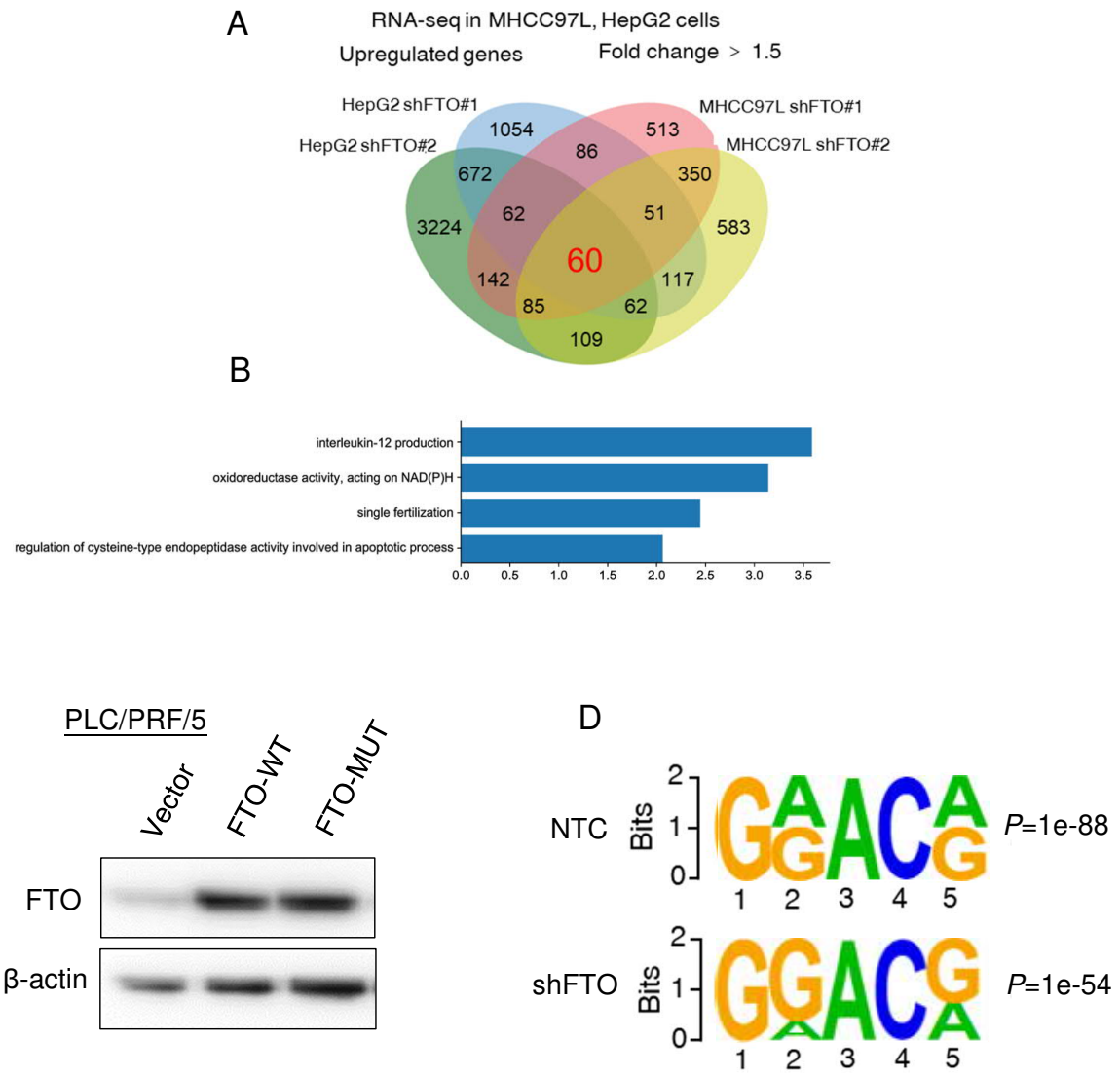

Supplementary Figure 4

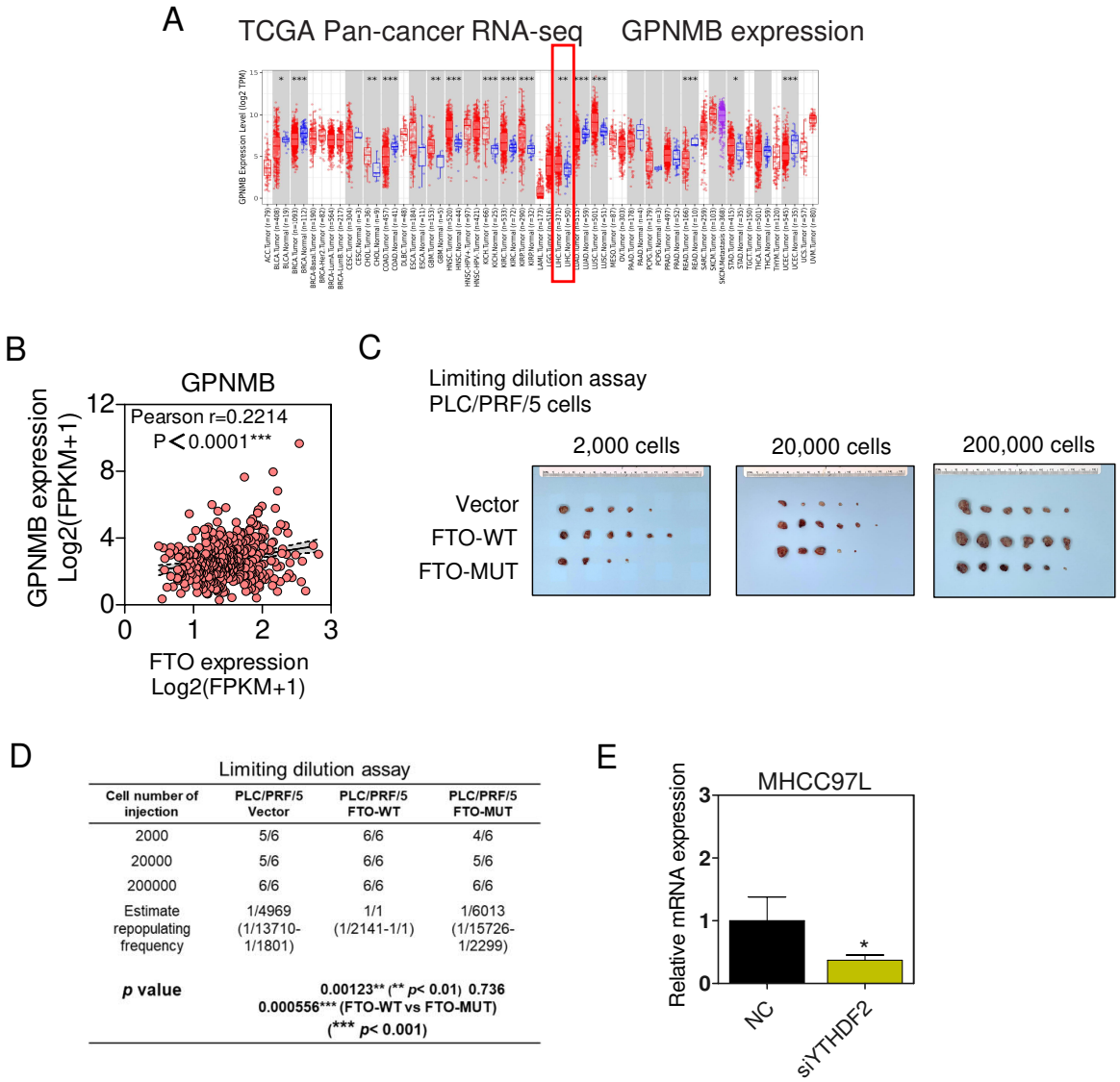

Cell number of injection	PLC/PRF/5 Vector	PLC/PRF/5 FTO-WT	PLC/PRF/5 FTO-MUT
2000	5/6	6/6	4/6
20000	5/6	6/6	5/6
200000	6/6	6/6	6/6
Estimate repopulating frequency	1/4969 (1/13710-1/1801)	1/1 (1/2141-1/1)	1/6013 (1/15726-1/2299)
***p* value**	**0.00123** (** *p*< 0.01) 0.736 0.000556*** (FTO-WT vs FTO-MUT) (*** *p*< 0.001)**		

Supplementary Figure 5

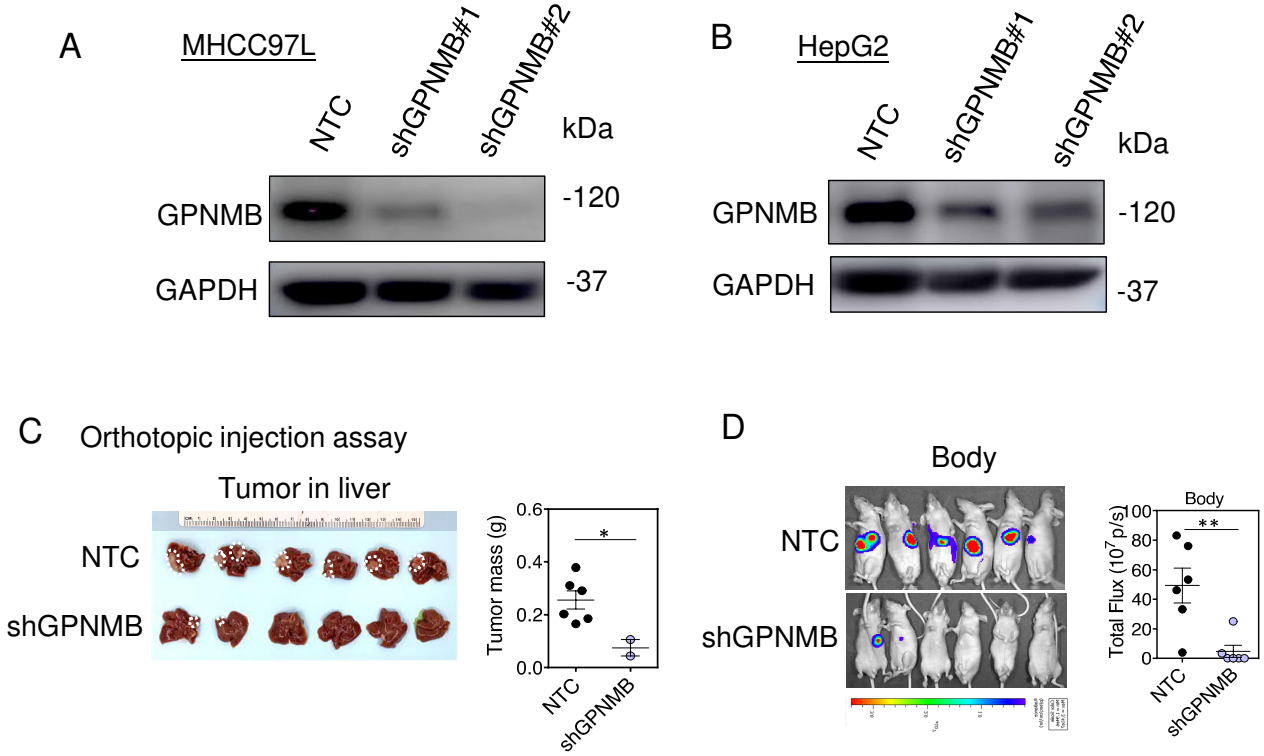

Supplementary Figure 6

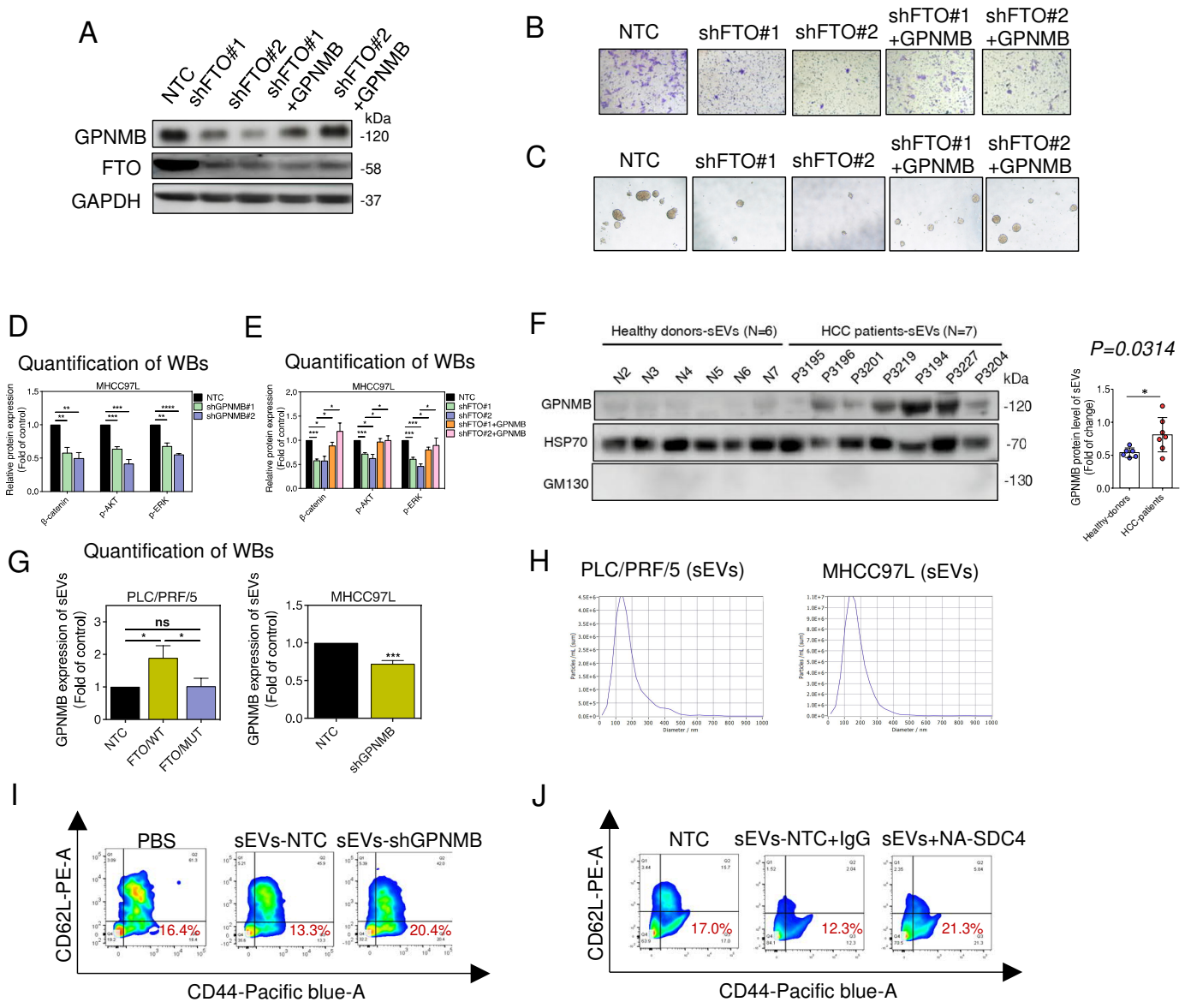

Supplementary Figure 7

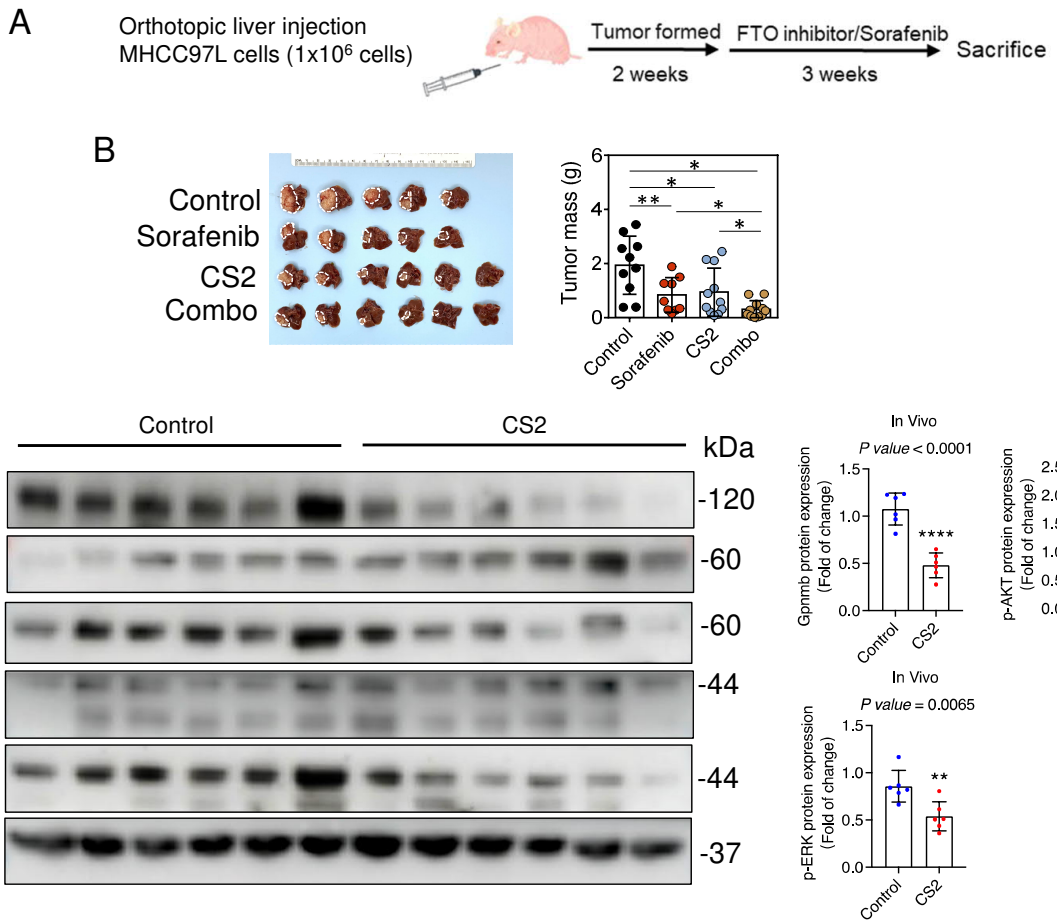

Supplementary Figure 8

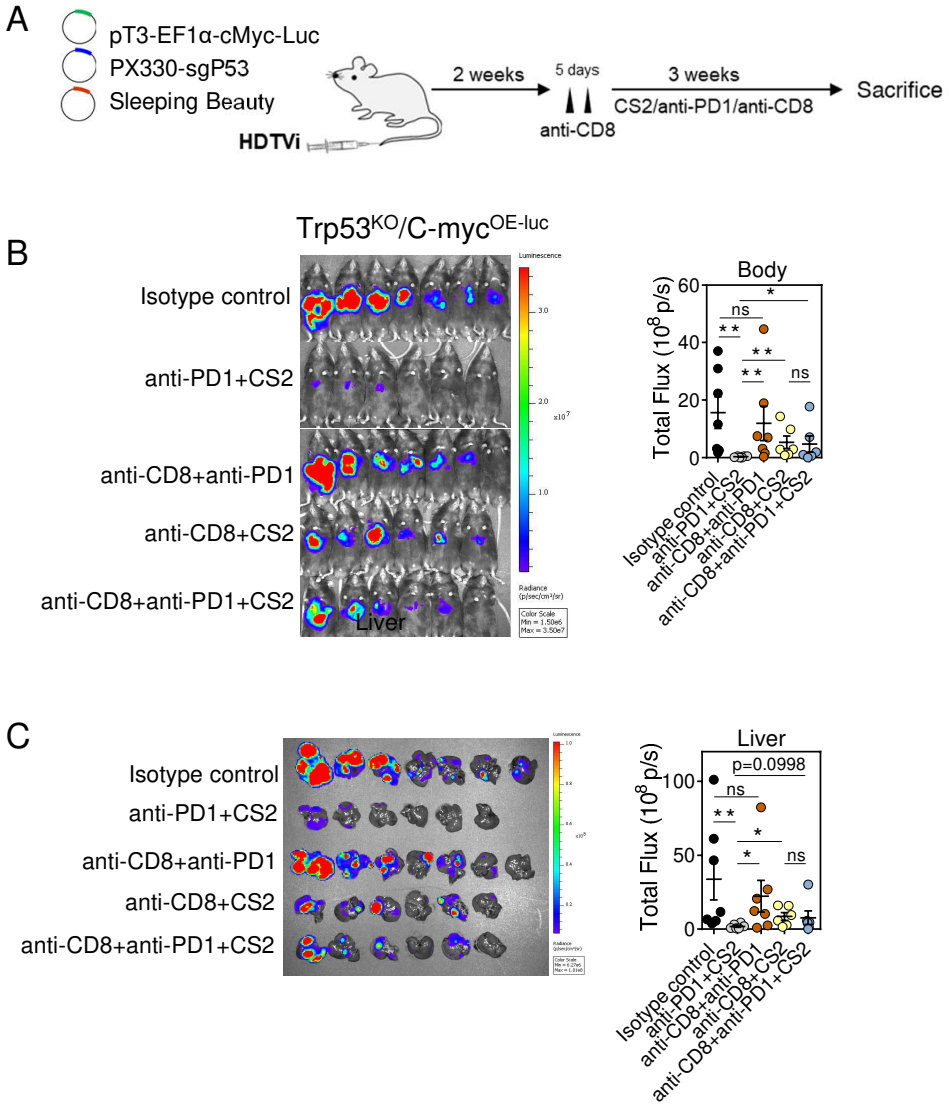

Supplementary file

Materials and Methods

Patient samples

A total of 95 patients with primary HCC from The University of Hong Kong-Queen Mary Hospital (HKU-QMH) were included in this study. The samples of these 95 patients were used to detect the FTO mRNA levels with qPCR. The overall and disease-free survival data were available in 88 and 69 of these patients, respectively. RNA-seq data of 41 patients was from our other independent HKU-QMH patient sample cohort and used to show the FTO mRNA levels. All patients are ethnic Chinese and had surgical resection at Queen Mary Hospital, Hong Kong. Primary HCC tumor samples and their corresponding non-tumorous (NT) liver samples were collected immediately after surgery and stored at -80°C. The use of clinical samples in this study was approved by the institutional review board of The University of Hong Kong and Hong Kong Hospital Authority.

Chemicals and antibodies

CS2 were obtained from Sigma-Aldrich (St. Louis, USA). Mouse anti-PD-1 antibody (clone: LTF-2) and IgG (clone: RMP1-14) control were purchased from BioXcell (Lebanon, NH, USA). Anti-YTHDF2, anti-beta Catenin, and anti-syndecan-4 antibodies were purchased from Abcam (Cambridge, UK). Syndecan-4 (5G9) blocking antibody was purchased from Santa Cruz (California, USA). Anti-m6A antibody was purchased from Synaptic Systems (Göttingen, Germany). Anti-human ERK1/2, Anti-human Phospho-ERK1/2, Anti-human AKT, Anti-human Phospho-AKT (Ser473) were purchased from Cell Signaling Technology (Danvers, USA). PMA (phorbol 12-myristate 13-acetate), IFNγ, Il-4 and IL-13 were obtained from Sigma-Aldrich.

Cell lines

Human HCC cell lines (HepG2, Hep3B, HuH7, PLC), normal liver cell line MIHA, mouse hepatoma cell line Hepa1-6 and human monocyte cell line THP-1 were obtained from American Type Culture Collection. Human HCC cell line 97L was a gift from Dr ZY Tang (Fudan University, Shanghai, China) and the STR authentication confirmed no contamination. HepG2, Hep3B and PLC were cultured in MEM containing 10% fetal bovine serum (FBS), while the others were cultured in DMEM supplemented with 10% FBS. Human bile duct carcinoma cell line HuCC-T1 and human colorectal adenocarcinoma cell line HCT-15 were also obtained from American Type Culture Collection. These cell lines were cultured in RPMI1640 containing 10% FBS.

Stable KD of HCC cells

A lentiviral-mediated approach was used to construct stable FTO or GPNMB KD HCC cell lines. Human ON-TARGETplus SMARTpool siRNA duplexes which target FTO or GPNMB and non-target control were purchased from Sigma-Aldrich. pLKO.1-puro vectors containing shRNAs targeting FTO (shFTO) or GPNMB (shGPNMB) and shNTC were stably transduced into HCC cell lines. Puromycin selection was performed to obtain stable expression of shRNAs and shNTCs. Sequences of all shRNAs are listed (Supplementary Table 3).

Animal models.

Limiting dilution assay was done by subcutaneously injecting 2×10^3, 2×10^4 and 2×10^5 HCC cells into the flanks of male BALB/cAnN-nu nude mice for 25-30 days. The tumor initiating capacity was analyzed by the confidence intervals (CIs) for 1/(stem cell frequency) using extreme limiting dilution analysis. Tumor incidence and tumor mass were recorded.

Orthotopic liver injection model was employed to investigate the tumor growth and progression. Briefly, 1×10^6 luciferase-labelled MHCC-97L cells were injected into the left lobes of livers of nude mice, whereas 3×10^6 luciferase-labelled mouse hepatoma Hepa1-6 cells were injected into left lobes of livers of C57BL/6 mice. Each experimental group had at least 6 mice. After 6 weeks for nude mice and 2 weeks for C57BL/6 mice, the mice were sacrificed and Xenogen IVIS 100 Imaging System (IVIS Spectrum In Vivo Imaging System, PerkinElmer, Waltham, MA) was utilized to visualize the liver tumor size and lung metastasis. Tumor mass and lung metastasis rate were recorded. Tumors from C57BL/6 mice were dissociated for detecting tumor infiltrating immune cells by flow cytometry.

For immune check point blockade (ICB) therapy, 3×10^6 Hepa1-6 cells were orthotopically injected into liver lobe of C57BL/6 mice. Five days later, all the mice were administrated with 250μg IgG control (LTF-2; BioXCell) or anti-PD-1 inhibitor (RMP1-14; BioXCell) intraperitoneally every 3 days for 8 days. Each experimental group had at least 6 mice. Xenogen IVIS 100 Imaging System was utilized to visualize the liver tumor size and lung metastasis. Tumor mass and lung metastasis rate were recorded.

For hydrodynamic tail-vein injection (HDTVi)-induced HCC model, sterile plasmid mix with a total volume corresponding to 10% of body weight was injected into lateral tail vein of 8-week old male C57BL/6 mice in 6-8 s. A total of 30 μg of CRISPR-Cas9 vector system carrying sgRNA targeting Trp53 ($Trp53^{KO}$) and EF1α overexpression vector carrying c-Myc ($C\text{-}Myc^{OE}$) and sleeping beauty (SB) transposon system was injected into lateral tail vein of 8-10-week old male C57BL/6 mice, as previous described [1]. Two weeks after delivery of plasmids, mice were treated intraperitoneally with vehicle control, anti-PD1 inhibitor (250μg per mouse), CS2 (5mg/kg) and combination of anti-PD1 and CS2 every 3 days for another 2 weeks. Each experimental group had at least 6 mice. Liver

weight was utilized to represent tumor mass here due to the multi-foci tumor formation of $Trp53^{KO}$ C-Myc^{OE} HDTVi model.

To deplete mouse CD8 T cells in vivo, $Trp53^{KO}$ C-$Myc^{OE\text{-}luc}$ HDTVi model was used. Two weeks after delivery of plasmids, C57BL/6 mice were administered with 2 doses of anti-CD8 antibody (BE0004-1, BioXcell) (250μg/mouse; i.p. injection; every 3 days) 5 days prior to CS2 (5mg/kg; i.p. injection; every 3 days) and/or anti-PD1 administration (250μg/mouse, i.p. injection; every 3 days). Mice were sacrificed at week 5 and Xenogen IVIS 100 Imaging System (IVIS Spectrum In Vivo Imaging System, PerkinElmer, Waltham, MA) was utilized to visualize the liver tumor size.

Flow cytometry for tumor infiltrating immune cell detection

Briefly, 2×10^5 dissociated tumors cells were stained by corresponding antibody for 1 hour in dark at room temperature according to manufacturer's instruction. The stained cells were washed with PBS buffer (2%FBS in PBS) and suspended in 200μl PBS buffer for detection by BioRad ZE5™ Cell Analyzer (Bio-Rad Laboratories, California, USA). Sources of the antibodies are provided in Supplementary Table 4.

Human T cell isolation and expansion

$CD8^+$ T cells were isolated from human PBMCs of healthy donors using commercial kit (Cat. No. 130-096-495; Miltenyi Biotec, Bergisch Gladbach, Germany) according to the manufacturer's instruction and expanded in vitro by adding recombinant IL2 (Cat.no.CTP0021; Thermofisher, Massachusetts, USA) and CD3/CD28 Dynabeads (Cat.no.11161D; Thermofisher).

T cell activation assay

1-2×10^5 isolated T cells were co-cultured with NTC or FTO-KD HCC cells for 5 days. T cells were harvested and the proportion of effector memory T cells ($CD44^+CD62L^-$) was detected by BioRad ZE5™ Cell Analyzer (Bio-Rad Laboratories, California, USA). Sources of the antibodies are provided in Supplementary Table 5.

T cell proliferation assay

1-2×10^5 isolated T cells were stained with 2μM of carboxyfluorescein succinimidyl ester (CSFE; Cat.no. C34554, Thermofisher) for 10 min and subsequently co-cultured with human HCC cells at a 1:1 ratio for 3 days. The counts of divided T cells were analyzed by flow cytometry with 488nm excitation, followed by gating the numbers of proliferated cells using FlowJo software and normalized to NTC group

Macrophage polarization assay

1×10^6 human monocyte THP-1 cells were induced to M0 differentiation with 200ng/ml PMA (phorbol 12-myristate 13-acetate) for 24 hours. Differentiated M0 macrophages were co-cultured with human HCC cells with or without FTO KD for 72 hours. mRNA expression of M1 and M2 markers was detected by qPCR. The primers are listed in Supplementary Table 2.

Macrophage recruitment assay

1×10^6 human monocyte THP-1 cells were induced to M0 differentiation with 200ng/ml PMA (phorbol 12-myristate 13-acetate) for 24 hours. Differentiated M0 macrophages were induced to M1 or M2 polarization by adding 20ng/mL IFNγ/LPS (Sigma-Aldrich) or 20ng/mL IL-4/IL-13 (Sigma-Aldrich), respectively, for another 48 hours. 2×10^5 M1 or M2 macrophages were seeded in the

upper chamber of transwell and co-cultured with human HCC cells in the lower chamber at a ratio of 1:1 for 72 hours. The macrophages in the upper chamber were fixed in methanol and stained with crystal violet. The cells having migrated through the upper chamber were counted by software Image J (National Institutes of Health, Bethesda, USA).

Histology

Mouse liver and lung tissues were dissected and sectioned for formalin fixation and paraffin embedding. Slides were stained with haematoxylin and eosin for histological analysis.

RNA extraction, reverse transcription PCR, and quantitative real-time PCR

Total RNA was extracted from clinical specimens or HCC cell lines using TRIzol reagent according to the manufacturer's protocol (Invitrogen, Carlsbad, CA). The RNA was then reverse-transcribed by the GeneAmp PCR Reagent Kit (Applied Biosystems, Foster City, CA). Quantitative real-time PCR (qRT-PCR) was performed with the use of Power SYBR Green PCR Master Mix (Applied Biosystems) with gene-specific primer sets and normalized to the internal control HPRT. The qPCR primer sequences are provided in Supplementary Table 2. All qRT-PCR reactions were done in triplicates.

Colony formation assay

For colony formation assay, 1000 cells were seeded into 6-well plates. After two weeks, formed HCC colonies were counted. Anchorage-independent growth was detected similarly as colony formation with plates coated with soft agar.

Sphere formation assay

1,000 cells were cultured in 0.25% methyl cellulose (Sigma-Aldrich) supplemented DMEM/F12 medium with 20ng/mL EGF (Life Technologies), 10ng/mL basic FGF, B27 (1:50, GIBCO), and 4μg/mL insulin in 24-well plates, which were coated with poly HEMA (Sigma-Aldrich). The cells were replenished with 30 μL supplementary medium every other day.

Cell proliferation assay

The proliferation rates of HCC cells were measured by cell counting. 1×10^3 cells in 100ul full medium were seeded in triplicate in 96-well culture plates. On the day of cell counting, cells were fixed with 50ul methanol for 5 minutes followed by staining with 50ul DAPI solution for 5 minutes. The cell counting was performed on ImageXpress pico system.

Transwell migration and invasion assays

For migration assay, 500ul conditioned medium containing 10% FBS from vector or shNTC control cells were collected and used as the chemoattractant in the bottom chamber in the 24-well plate. 1×10^5 cells were re-suspended in 100μl serum-free medium and seeded into the upper transwell with an 8um-pore size membrane (Millipore). After 18 hours of incubation, the migrated cells were fixed with methanol for 15 minutes and stained with crystal violet for 20 minutes. For cell invasion assay, the transwells were coated with Matrigel (BD Biosciences, San Jose, CA) on the upper surface of transwell chamber and kept in the incubator for 1 hour before cell seeding. Photographs of three randomly selected fields of the stained migrated or invaded cells were captured and the total numbers of migrated and invaded cells were counted. The experiments were repeated independently three times.

Isolation of sEVs from cell culture medium

For isolation of sEVs from cell culture supernatants, HCC cells were cultured in medium with 10% sEV-depleted FBS, which was prepared by 100,000×g centrifugation overnight (⩾12h) at 4 °C (Himac, CP100NX Ultracentrifuges). sEVs were purified by differential centrifugation after the cell culture supernatant were collected. Briefly, cell culture supernatants were centrifuged at 2000×g for 15 min to remove cell debris and dead cells. The supernatant was centrifugated at 20,000×g for 30 min at 4 °C to remove microvesicles and passed through 0.22 μm filter followed by ultracentrifugation at 100,000×g for 2 h at 4 °C to collect sEVs. The sEVs were washed with PBS and collected by ultracentrifugation at 100,000×g for another 2 h at 4 °C.

sEV characterization

The morphology and integrity of sEVs were observed by electron microscopy (Philips CM100 transmission electron microscope; FEI Company). Target proteins present on EVs were determined by immunogold staining followed by visualizing by transmission electronic microscopy. Protein of isolated sEVs was examined by western blotting with sEV specific markers CD63 (Sigma-Aldrich), CD81 (Abcam), CD9 (Abcam), HSP70 (Abcam), Alix (Santa Cruz), and sEVs negative markers GM130 (Abcam). The size distribution of sEVs and particle concentration was measured by ZetaView BASIC NTA PMX-120 (Particles Metrix GmbH).

Proteinase K treatment

A total of 25 μg of sEVs were subjected to Proteinase K treatment, which effectively stripped surface proteins without compromising the integrity of the sEVs. Proteinase K was stocked at a

concentration of 20 mg/mL and was diluted 1000-fold to a working concentration of 20 μg/mL prior to use. Each sample was brought up to a total volume of 100 μL and incubated at 37℃ for exactly 5 minutes. The reaction was stopped by adding 1 mL of sEV-free full medium to each sample. The sample was then purified by ultracentrifugation at 100,000×g for 1.5 hours, after which the supernatant was completely removed, and the pellet was dissolved in 50 μL of PBS. To prepare for Western blotting, 10 μL of 6×loading buffer was mixed with each sample and boiled at 95℃ for 10 minutes. An equal volume of samples was loaded for Western blotting. Tetraspanin protein CD63 and heat shock protein HSP70 were used as representative membrane and inner proteins, respectively. The pattern of the target protein was compared to the representative proteins to determine the location of the target protein on the sEVs.

Western blotting analysis

Quantified protein lysates were resolved on SDS-PAGE, transferred onto a polyvinylidenedifluoride (PVDF) membrane (Bio-Rad), and blocked with 5% non-fat milk in Tris-buffered saline-Tween 20 (TBST) for 1 h at room temperature. The blocked membrane was then incubated with primary antibody diluted in 5% bovine serum albumin in TBST at 4 °C overnight. Band intensities of western blot were analyzed using ImageJ. Antibodies used in this study are listed in Supplementary Table 4.

m6A Dot Blot assay

To determine the global m6A abundance, m6A dot blot assays were employed with total RNA as described previously[2]. In brief, 50 ul RNA samples was mixed with 150 ul RNA incubation buffer, followed by denatured at 65 °C for 5 minutes. 200ml of chilled 20×SSC buffer was added and

mixed well before samples were loaded onto the Amersham Hybond-N+ membrane (RPN303B, GE Healthcare) with a Bio-Dot Apparatus (Bio-Rad). After crosslinking under 254 nm UV for 1 h, the membrane was stained with methyl blue and the image was captured. The membrane was then washed with 1×PBST buffer (PBST01-02, Bioland Scientific LLC), blocked with 5% non-fat milk and incubated with rabbit anti-m6Aantibody (1:2000, 202003, Synaptic Systems) overnight at 4°C. After washing, the membrane was incubated with HRP-conjugated goat anti-rabbit IgG (ab6721, Abcam) for 1 hour at room temperature and was developed with Amersham ECL Prime Western Blotting Detection Reagent (45-010-090, Fisher Scientific).

Transcriptome sequencing

Transcriptome sequencing of stable FTO KD HepG2 and 97L cells and their non-target controls (NTC) were performed with HiSeq-1500. PolyA$^+$ messenger RNA (mRNA) library was constructed with KAPA Stranded mRNA-Seq Kit. RNA-data were analyzed as previously described[3-5]. In brief, sequencing reads were aligned to reference human genome (hg38) by HISAT2. Transcripts were assembled by StringTie and the expression level of individual genes was identified as fragments per kilobase per million (FPKM). Gene ontology and pathway analyses were carried out.

m6A-methylated RNA immunoprecipitation (MeRIP) assay and m6A sequencing

Total RNAs were first extracted from stable FTO KD HepG2 and 97L cells and their corresponding NTCs. RNAs were treated with DNase according to TURBO DNA-freeTM Kit (ThermoFisher) protocol to avoid DNA contaminations. RNA concentration was adjusted to 1μg/μl with nuclease-free water. RNA was chemically fragmented into ~100nt size and fragmented RNA was incubated with m6A antibody for immunoprecipitation according to the standard protocol of Magna MeRIP™

m6A Kit (Merck Millipore). For high-throughput sequencing, purified RNA fragments from m6A-MeRIP were used for library construction with NEBNext Ultra RNA library Prep kit from Illumina and sequenced with Illumina HiSeq 2000. Library preparation and high-throughput sequencing were done by Novogene, Beijing, China.

All the IP and Input samples were sequenced by Illumina Novaseq platform with paired end 150-bp read length. Quality control of raw data was performed with FastQC (v0.11.8) according to Q30 standards[6]. Clean fastq reads were aligned to the human reference genome (GRCh38/hg38; Ensemble version 103) via HISAT2 (v2.2.1)[7] aligner with default settings after quality control by Cutadapt (v2.10)[8] and Trimmomatic (v0.38)[9]. Only the reads with mapping quality score (MAPQ) ≥20 were kept for the downstream analysis. For MeRIP-seq, the MACS3 (v 3.0.0a7; p-value < 0.05, call-summit, no model, extsize 50)[10] software was used to identity m6A methylation sites (peaks) based on its paired m6A-RIP/input data from the aligned reads with fold changes cut-off > 1.5. All m6A peaks were intersected in a pairwise fashion among two or three replicates or between two conditions using the BedTools package[11]. The m6A-enriched motifs were identified by using HOMER (v4.7) findMotifsGenome.pl with the parameter '-rna -len 5,6'. All the peaks annotated in mRNAs were used as target sequences, and exon sequences except for the peak-containing sequences were used as the background sequences. The p-values for all motifs were calculated and reported by Homer under the assumptions described at the Homer website (http://homer.ucsd.edu/homer/motif/). Visualization of m6A peaks were performed by IGV (Integrative Genomics Viewer) software (v2.14.0)[12].

Statistics

Statistical analyses were performed using GraphPad Prism 6.0 software (GraphPad Software Inc.). One-way ANOVA with Dunnett comparison test for more than two groups or Student's t tests were used to compare the mean values of two groups. For in vitro functional assays, data were expressed as mean ± SD. For in vivo experiments, data were expressed as mean ± SD followed by either Unpaired t-test or Mann-Whitney test. Statistical significance was defined as *P<0.05, ** P<0.01, and ***P<0.001.

Supplementary Figure legend

Supplementary Figure S1. **Expression FTO in different HCC cell lines and expression of cancer stemness markers upon FTO KD.** (A) TCGA database shows FTO expression in different types of cancer. (B) The etiology of HCC patients. (C) STR authentication of 97L cells. (D) FTO mRNA and protein level in five HCC cell lines and an immortalized normal liver cell line (MIHA) by qPCR and western blotting. (E) The FTO KD efficiency at mRNA level in 97L and HepG2 cells by qRT-PCR. (F) The mRNA levels of cancer stemness genes upon FTO KD. (t-test, mean ± SD, *P < 0.05, **P < 0.01, ***P < 0.001)

Supplementary Figure S2. Enhanced immune response in tumor microenvironment upon FTO KD in vivo. (A)-(C) Representative flow cytometry histogram and quantification of the proportion of tumor infiltrating macrophages ($CD45^+/F4/80^+$), M1 ($CD45^+F4/80^+CD86^+$), and M2 macrophages ($CD45^+F4/80^+CD163^+$), respectively. (D) CSFE staining showing FTO enhanced human $CD8^+$ T cell proliferation upon co-culturing with FTO KD HCC cells. (E) mRNA expression of M1 and M2 macrophage-related genes upon co-culturing with HCC cells (NTC, shFTO#1 and shFTO#2). (t-test, mean ± SD, *P < 0.05, **P < 0.01, ***P < 0.001)

Supplementary Figure S3. RNA-seq and MeRIP assays with FTO KD in 97L and HepG2 cells. (A) Venn diagram and (B) GO Biological Processes Annotation Analysis showing upregulated genes by >1.5 folds upon FTO KD in HepG2 and 97L cells. (C) Successful overexpression FTO-WT and FTO-MUT at protein level in PLC cells by western blotting. (D) m6A motif detected by the HOMER motif analysis with m6A-seq data in 97L cells with or without FTO KD. (t-test, mean ± SD, *P < 0.05, **P < 0.01, ***P < 0.001)

Supplementary Figure S4. Promotion of HCC tumor growth by FTO was dependent on its demethylase activity. (A) The TCGA database shows significant upregulation of GPNMB expression in multiple cancer types. (B) GPNMB expression was positively correlated with FTO expression in TCGA HCC cohort. (C) Limiting dilution assay showing tumors derived from subcutaneous xenografts by injection of 2×10^3, 2×10^4 and 2×10^5 PLC cells. (D) The tumor incidence rate for each group was recorded at the end of the experiments after 4 weeks. The tumor initiating capacity was analyzed by the confidence intervals (CIs) with the formula of CI = 1/ (stem cell frequency). (E) KD efficiency of YTHDF2 siRNA in 97L cells was measured by qRT-PCR. (t-test, mean ± SD, *P < 0.05, **P < 0.01, ***P < 0.001)

Supplementary Figure S5. Successful KD of GPNMB in HepG2 and 97L cells. (A), (B) Stable GPNMB KD models established with two independent shRNA sequences in 97L and HepG2 cells. The protein level of GPNMB was detected by western blotting. (C) Liver with tumors derived from orthotopic injection of 97L cells (NTC and shGPNMB) and the tumor mass. n=6 in each group. (D) Bioluminescence images of mice with quantification of their bioluminescent intensities. (t-test, mean ± SD, *P < 0.05, **P < 0.01)

Supplementary Figure S6. FTO promoted cell proliferation and sphere formation through upregulating GPNMB in HCC. (A) Successful overexpression of GPNMB in FTO-KD HCC cells, detected by western blotting. (B) Migration and (C) sphere formation assays showing abrogation of the suppression by FTO KD with overexpression of GPNMB. (D), (E) Quantification for bands in the Western blots. (F) GPNMB expression on sEVs derived from HCC patients' and healthy donors' plasma. (G) Quantification for bands in the Western blots. (H) Size distribution of sEVs derived from 97L and PLCPRF/5 cells, as measured by ZetaView Particle Tracking Analyzer. (I), (J) Degree of activation of effector memory T cells ($CD44^{+}CD62L^{-}$) by flow cytometry.

Supplementary Figure S7. CS2 sensitized HCC cells to Sorafenib treatment in vivo. (A) A schematic summary of Sorafenib treatment in vivo. Orthotopic 97L cell-derived xenograft tumors were treated with vehicle control, sorafenib, CS2, and combined sorafenib and CS2. (B) Tumors in the livers and the tumor masses. (C) Protein expression of GPNMB, AKT/p-AKT and ERK/p-ERK in mouse tumor tissues by western blotting.) (D) Proportions of macrophages in tumor tissues by flow cytometry. (t-test, mean ± SD, *P < 0.05, **P < 0.01).

Supplementary Figure S8. Depletion of CD8 T cells in mice abrogated the anti-tumor effect of CS2/anti-PD1. (A) A schematic summary of anti-CD8, FTO inhibitor CS2 and anti-PD-1 treatment in hydrodynamic tail vein injection (HDTVi) (p53 KO/c-Myc-luc) model. (B), (C) Bioluminescent images and quantification of their bioluminescent intensities. (one-way ANOVA followed by Dunnett comparison test, mean ± SD, *P < 0.05, **P < 0.01, ***P < 0.001).

Supplementary References:

1 Ho, D. W. H. *et al.* Single-cell RNA sequencing shows the immunosuppressive landscape and tumor heterogeneity of HBV-associated hepatocellular carcinoma. *Nature Communications* **12**, doi:ARTN 368410.1038/s41467-021-24010-1 (2021).

2 Su, R. *et al.* R-2HG Exhibits Anti-tumor Activity by Targeting FTO/m6A/MYC/CEBPA Signaling - ScienceDirect. (2018).

3 Ho, D. W.-H. *et al.* Single-cell transcriptomics reveals the landscape of intra-tumoral heterogeneity and stemness-related subpopulations in liver cancer. *Cancer letters* **459**, 176-185 (2019).

4 Ho, D. W.-H. *et al.* Single-cell RNA sequencing shows the immunosuppressive landscape and tumor heterogeneity of HBV-associated hepatocellular carcinoma. *Nature Communications* **12**, 3684 (2021).

5 Ho, D. W.-H., Lam, W.-L. M., Chan, L.-K. & Ng, I. O.-L. Investigation of Functional Synergism of CENPF and FOXM1 Identifies POLD1 as Downstream Target in Hepatocellular Carcinoma. *Frontiers in Medicine* **9**, 860395 (2022).

6 Andrews, S. (Babraham Bioinformatics, Babraham Institute, Cambridge, United Kingdom, 2010).

7 Kim, D., Langmead, B. & Salzberg, S. L. HISAT: a fast spliced aligner with low memory requirements. *Nature methods* **12**, 357-360 (2015).

8 Martin, M. Cutadapt removes adapter sequences from high-throughput sequencing reads. *EMBnet. journal* **17**, 10-12 (2011).

9 Bolger, A. M., Lohse, M. & Usadel, B. Trimmomatic: a flexible trimmer for Illumina sequence data. *Bioinformatics* **30**, 2114-2120 (2014).

10 Zhang, Y. *et al.* Model-based analysis of ChIP-Seq (MACS). *Genome biology* **9**, 1-9 (2008).

11 Quinlan, A. R. & Hall, I. M. BEDTools: a flexible suite of utilities for comparing genomic features. *Bioinformatics* **26**, 841-842 (2010).

12 Thorvaldsdóttir, H., Robinson, J. T. & Mesirov, J. P. Integrative Genomics Viewer (IGV): high-performance genomics data visualization and exploration. *Briefings in bioinformatics* **14**, 178-192 (2013).

Supplementary Table 1.

Clinicopathological correlation of FTO overexpression in HCC patient samples.

Parameters	FTO overexpression (n=37)	FTO normal and underexpression (n=56)	*P* *
Gender			0.238
Male	30 (32.3%)	39 (41.9%)	
Female	7 (7.5%)	17 (18.30%)	
Mean age (range) ^	51. 6(16-74)	56.3 (24-74)	0.081
Tumor size			0.347
>5cm	18 (22.8%)	33 (41.8%)	
≤5cm	13 (16.5%)	15 (19.0%)	
Background liver disease			0.115
Normal and Chronic hepatitis	12 (15.0%)	27 (33.8%)	
Cirrhosis	20 (25.0%)	21 (26.3%)	
Liver invasion			0.639
Presence	14 (17.7%)	17 (21.5%)	
Absence	18 (22.8%)	30 (38.0%)	
Tumor microsatellite formation			0.385
Presence	22 (25.6%)	27 (31.4%)	
Absence	13 (15.1%)	24 (27.9%)	
Tumor encapsulation			0.644
Presence	12 (14.3%)	16 (19.0%)	
Absence	21 (25.0%)	35 (41.7%)	
Venous invasion			0.529
Presence	23 (24.7%)	31 (33.3%)	
Absence	14 (15.1%)	25 (26.9%)	
Cellular differentiation			0.358
Edmondson grade I-II	16 (20.2%)	18 (22.8%)	
Edmondson grade III-IV	16 (20.2%)	29 (36.7%)	
TNM staging			**0.000029***
I-II	2 (2.4%)	25 (30.1%)	
III-IV	31 (37.3%)	25 (30.1%)	

* Fisher exact test

^ t-test

Supplementary Table 2

Primer sequences used for qRT-PCR analysis.

Target gene		Sequence (5'-3')
Human FTO	Forward	ACAACGGACAAGATGAAGTGGA
	Reverse	ATCCCTGCCTTCGAGATGAG
Human AKT3	Forward	TGGATGCCTCTACAACCCATCA
	Reverse	TGTGTGCCACTTCATCCTTTGC
Human PDGFB	Forward	CTCGATCCGCTCCTTTGATGA
	Reverse	CGTTGGTGCGGTCTATGAG
Human RORO4	Forward	CCCTGTGCTTGGAACTCAGTG
	Reverse	CGCTGATGTACCCATAGGTGG
Human GPNMB	Forward	AAGTGAAAGATGTGTACGTGGTAACAG
	Reverse	TCGGATGAATTTCGATCGTTCT
Human FZD8	Forward	TGGAGTGGGGTTACCTGTTG
	Reverse	AGCGGCTTCTTGTAGTCCTC
Human SEMA3G	Forward	GGGTCTGTGCTCAAAGTCATCG
	Reverse	AAGTCCCACTGCCTCTTCTTCC
Human YTHDF2	Forward	TAGCCAACTGCGACACATTC
	Reverse	CACGACCTTGACGTTCCTTT
Human CD68	Forward	ATTCACCAGTTCTGCCCACC
	Reverse	GCTTCCCTGGACCTTGGTTT
Human CD80	Forward	TGCTGGCTGGTCTTTCTCAC
	Reverse	GTCCGGTTCTTGTACTCGGG
Human CD86	Forward	CCCCAGTGCACTATGGGAC
	Reverse	CAGGGTCCAACTGTCCGAAT
Human CD204	Forward	CGAAAGTTCGACTGGTCGGT
	Reverse	TGTCCCCCATTGCCGAATTT
Human CD206	Forward	CATCAGGGTGCAAGGAAGGT
	Reverse	TCCATCCGTCCAAAGGAACG
Human CD163	Forward	TCCTTGTGGGATTGTCCTGC
	Reverse	ATGGGAATTTTCTGCAAGCCG
Human SMO	Forward	TGGTCACTCCCCTTTGTCCTCAC
	Reverse	GCACGGTATCGGTAGTTCTTGTAGC
Human NANOG	Forward	CCTGTGATTTGTGGGCCTG
	Reverse	GACAGTCTCCGTGTGAGGCAT
Human OCT4	Forward	CTTGCTGCAGAAGTGGGTGGAGGAA
	Reverse	CTGCAGTGTGGGTTTCGGGCA
Human GAPDH	Forward	ACAACGGACAAGATGAAGTGGA
	Reverse	ATCCCTGCCTTCGAGATGAG
Human HPRT	Forward	CTTTGCTGACCTGCTGGATT
	Reverse	CTGCATTGTTTTGCCAGTGT

Supplementary Table 3.
List of shRNA sequences used in this study.

Target gene	Species	Sequence (5'-3')
shFTO#1	Human	CCCATTAGGTGCCCATATTTA
shFTO#2	Human	TCACCAAGGAGACTGCTATTT
shGPNMB#1	Human	CACAAGGAATACAACCCAATA
shGPNMB#2	Human	CGCACAAGTGAAAGATGTGTA
shFTO#1	Mouse	TTGAAAGAGGAGCCCTATTTC
shFTO#2	Mouse	GTCTCGTTGAAATCCTTTGAT
shNTC	H & M	CAACAAGATGAAGAGCACCAA

Supplementary Table 4.

List of antibodies used in this study.

Antibody	Application	Source	Cat No.
m6A (N6-methyladenosine) antibody	Dot bolt, WB	Synaptic Systems	202003
Anti-FTO antibody	WB	Abcam	ab126605
Recombinant Anti-GPNMB antibody	WB, Co-IP, Immunogold	Abcam	ab235873
Recombinant Anti-beta Catenin antibody	WB	Abcam	ab32572
Anti-Syndecan 4 antibody	WB	Abcam	ab74139
Syndecan-4 Antibody (5G9)	Neutralization	Santa Cruz	sc-12766
Anti-Akt	WB	Cell signaling	9272
Anti-phospho-Akt (Ser473)	WB	Cell signaling	9271
Anti-p44/42 MAPK (ERK1/2)	WB	Cell signaling	4695
Anti-Phospho-p44/42 MAPK (ERK1/2)	WB	Cell signaling	4370
Anti-CD63	WB	Sigma-Alrich	SAB2109138
Anti-CD63	Immunogold	Abcam	ab271286
Anti-CD9	WB	Abcam	ab92726
Anti-CD81	WB	Abcam	ab79559
Anti-ALIX	WB	Santa Cruz	53540
Anti-HSP70	WB	Abcam	ab181606
Anti-GM130	WB	Abcam	ab52649
Anti-GFP (B-2)	WB, Co-IP	Santa Cruz	sc-9996
Donkey Anti-Rabbit IgG H&L	Immunogold	Abcam	ab105294
Goat Anti-Mouse IgG H&L	Immunogold	Abcam	ab27241
Normal rabbit IgG	Co-IP	Santa Cruz	sc-2027
Normal mouse IgG	WB	Santa Cruz	sc-3877

Human CD44	Flow cytometry	Miltenyibiotec	130-113-337
Human CD62L	Flow cytometry	Biolegend	304840
Mouse CD45	Flow cytometry	Biolegend	103128
Mouse CD8	Flow cytometry	Biolegend	126606
Mouse CD4	Flow cytometry	Biolegend	100451
Mouse CD279 (PD-1)	Flow cytometry	Biolegend	135216
Mouse F4/80	Flow cytometry	Biolegend	157304
Mouse CD86	Flow cytometry	Biolegend	105110
Mouse CD163	Flow cytometry	Biolegend	155320
Isotype Control In vivo blockade (IgG)	In vivo treatment	BioXcell	BP0090
InVivoMAb anti-mouse PD-1 (CD279)	In vivo treatment	BioXcell	BE0146
InVivoMAb anti-mouse CD8α	In vivo treatment	BioXcell	BE0004-1

Supplementary Table 5.

List of reagents used in this study.

Antibody	Source	Cat No.
RNA Fragmentation Reagents	Thermo Fisher	AM8740
Methyl Blue	Millipore Sigma	M6900
Amersham Hybond-N+ membrane	GE Healthcare	RPN119B
Brequinar (CS2)	Sigma-Alrich	508321
Magna MeRIP m6A Kit	Millipore	17-10499
CD8+ T Cell Isolation Kit, human	Miltenyi biotec	130-096-495
Dynabeads™ Human T-Activator	Thermofisher	11131D
CD3/CD28	Thermofisher	PHC0021
Recombinant Human IL-2 Protein	Goldbio	Luck-1G
D-Luciferin Firefly, potassium salt		